HHS Public Access

Author manuscript

Nature. Author manuscript; available in PMC 2024 November 20.

Published in final edited form as:

Nature. 2023 September ; 621(7979): 543–549. doi:10.1038/s41586-023-05995-9.

Intrinsic dopamine and acetylcholine dynamics in the striatum of mice

Anne C. Krok[1], **Marta Maltese**[1,#], **Pratik Mistry**[1,#], **Xiaolei Miao**[2,3], **Yulong Li**[3], **Nicolas X. Tritsch**[1,*]

[1]Neuroscience Institute, New York University Grossman School of Medicine; New York, NY 10016, U.S.A., and Fresco Institute for Parkinson's and Movement Disorders, New York University Langone Health, New York, NY 10016, U.S.A

[2]Department of Anesthesiology, Beijing Chao-Yang Hospital, Capital Medical University, Beijing, China

[3]State Key Laboratory of Membrane Biology, Peking University School of Life Sciences, Beijing, China

Abstract

External rewards like food and money are potent modifiers of behavior[1,2]. Pioneering studies established that these salient sensory stimuli briefly interrupt the tonic discharge of neurons that produce the neuromodulators dopamine (DA) and acetylcholine (ACh): midbrain DA neurons (DANs) fire a burst of action potentials that broadly elevates DA in the striatum[3,4] at the same time as striatal cholinergic interneurons (CINs) produce a characteristic pause in firing[5,6]. These phasic responses are thought to create unique, temporally-limited conditions that motivate action and promote learning[7–11]. However, the dynamics of DA and ACh outside explicitly-rewarded situations remain poorly understood. Here we show that extracellular DA and ACh levels fluctuate spontaneously and periodically at approximately 2 Hz in the striatum of mice and maintain the same temporal relationship relative to one another as that evoked by reward. We show that this neuromodulatory coordination does not arise from direct interactions between DA and ACh within the striatum. Instead, we provide evidence that periodic fluctuations in striatal DA are inherited from midbrain DANs, while striatal ACh transients are driven by glutamatergic inputs, which act to locally synchronize the spiking of CINs. Together, our findings reveal that striatal neuromodulatory dynamics are autonomously organized by distributed extra-striatal afferents. The dominance of intrinsic rhythms in DA and ACh offers novel insights for explaining how

*Correspondence and requests for materials should be addressed to N.X.T., nicolas.tritsch@nyulangone.org.
#equal contribution

Author contributions

A.C.K and N.X.T conceived of the project, designed and performed experiments, analyzed and interpreted the data, and wrote the manuscript. A.C.K and P.M wrote code for photometry data acquisition and analyses, M.M performed dopamine neuron lesions and helped with photometry data collection and analyses, X.M and Y.L performed experiments to determine the kinetics of ACh3.0 and provided the GRAB sensors rDA1m and ACh3.0.

Code availability

All code related to this study was developed in MATLAB and is available at https://github.com/ackrok/Krok-etal_2023

Competing interests

Y.L is listed as an inventor on a patent application (PCT/CN2018/107533) describing GRAB probes. The other authors declare no competing interests.

reward-associated neural dynamics emerge and how the brain motivates action and promotes learning from within.

Rewards and the sensory cues that predict their availability elicit brief changes in the release of the neuromodulators DA and ACh. These phasic responses are thought to stand out from the basal, steady concentration of DA and ACh that brain circuits normally bathe in to affect behavior. In the mammalian striatum, rewards evoke a phasic increase in extracellular DA[3,4] and a phasic decrease in ACh[5,6], the coincidence of which is critical for DA to act as a teaching signal, as muscarinic M4 receptors oppose D1 receptor-dependent synaptic plasticity on direct-pathway striatal projection neurons (SPNs) [12,13]. Recent studies have also implicated phasic DA elevations in the initiation and invigoration of self-paced movements[14–17], and ACh has been proposed to help striatal circuits distinguish between DA signals related to motor performance and learning[9–11,18,19]. However, the dynamics of extracellular DA and ACh levels *in vivo* remain unknown. Because DA and ACh interact extensively in the striatum without necessarily engaging somatic spiking[20–25], addressing this question requires approaches that directly and simultaneously report DA and ACh levels on sub-second time scales.

To reveal the dynamics of striatal DA and ACh, we imaged the D2 receptor-based red fluorescent GRAB-DA indicator rDA1m[26] and the muscarinic M3 receptor-based green fluorescent GRAB-ACh indicator ACh3.0[27] concurrently from the dorsolateral striatum (DLS) of mice head-fixed on a cylindrical treadmill using fiber photometry (Fig. 1a and Extended Data Fig. 1). These sensors display comparable kinetics in the hundred-millisecond range when reporting striatal release of DA and ACh *in vivo*[26] (Extended Data Fig. 2). Mice spontaneously alternated between bouts of immobility and locomotion, and on a subset of recording sessions were provided with uncued water rewards. As expected, rewards evoked phasic changes in the fluorescence of both sensors reminiscent of the characteristic discharge of midbrain DANs[3,4] and striatal CINs[5,6] (Fig. 1b–e and Extended Data Fig. 3). On average, rDA1m showed a sharp increase in fluorescence (mean amplitude: 9.9 ± 1.0 % ΔF/F; n = 13 mice) that decayed back to baseline within 1.5 s, whereas ACh3.0 showed a phasic dip in fluorescence below a stable baseline (mean amplitude: −4.4 ± 0.5 % ΔF/F; mean duration: 298 ± 21 ms) preceded by a brief increase in fluorescence (mean amplitude: 2.9 ± 0.7 % ΔF/F). These events appeared in a sequence, starting with the ACh3.0 peak followed 82 ± 5 ms later by the rDA1m peak, itself followed by the dip in ACh3.0 fluorescence (time to trough: 200 ± 17 ms) (Fig. 1f, g). These data are consistent with the sequence of reward-evoked action potential responses observed from putative DANs and CINs in rodents and primates[3–6].

The fluorescence of rDA1m and ACh3.0 also increased during locomotion, with ACh3.0 peaking near the time of maximum positive acceleration and rDA1m peaking shortly thereafter (Fig. 1b and Extended Data Fig. 4), consistent with recent reports using genetically-encoded calcium indicators to monitor the activity of midbrain DANs and striatal CINs in mice[14,19]. Together, these data confirm our ability to detect and isolate phasic changes in striatal DA and ACh from simultaneous photometric recordings.

DA and ACh fluctuate spontaneously

rDA1m and ACh3.0 fluorescence signals also showed large, periodic fluctuations during periods of immobility and in the absence of overt sensory stimuli that were not apparent in session-averaged data (Fig. 1b, c, h, l and Extended Data Fig. 3a, m, n). These spontaneous signal fluctuations, which occurred most prominently in the 0.5–4 Hz frequency band (mode for DA: 2.0 ± 0.2 Hz; ACh: 1.8 ± 0.2 Hz; Fig. 1j, n) were also observed before mice ever received rewards on the treadmill as well as in an open field arena (Extended Data Fig. 5), but not in mice expressing green fluorescent protein (GFP) or tdTomato (Fig. 1i, m), confirming that they do not reflect hemodynamic, movement, or signal processing artifacts. In mice expressing rDA1m alone, spontaneous fluorescence transients during immobility were reversibly blocked following systemic administration of the D2 receptor (D2R) antagonist sulpiride (n = 8 mice) and were entirely absent following infusion of the toxin 6-hydroxydopamine (6-OHDA) in the substantia nigra pars compacta (SNc; n = 6 mice; Fig. 1h, i, k), showing that rDA1m fluorescence transients during immobility reflect DA release from midbrain DANs. In ACh3.0-expressing mice, spontaneous fluorescent transients disappeared upon treatment with the muscarinic ACh receptor (mAChR) antagonist scopolamine (n = 5 mice) and were not detected in mice in which the ACh synthetic enzyme choline acetyltransferase (ChAT) is conditionally knocked out of forebrain cholinergic neurons ($ChAT^{floxed/floxed}$;$Nkx2.1^{Cre}$ mice, referred to as ChAT $cKO^{forebrain}$; n = 5 mice; Fig. 1l, m, o), indicating that ACh3.0 fluctuations reflect spontaneous changes in ACh release from local CINs and not from brainstem cholinergic afferents. Together, these data show that striatal circuits constantly undergo large, periodic increases and decreases in extracellular DA and ACh levels originating from midbrain DAN axons and striatal CINs, respectively.

DA and ACh are constantly phase-shifted

Striatal neurons co-express receptors for DA and ACh that engage competing intracellular signaling pathways[12,13,28]. The net impact of phasic changes in DA and ACh levels on striatal function therefore depends on their relative timing and amplitude. During rewards, DA and ACh were negatively correlated (Pearson cross-correlation coefficient r = –0.48 ± 0.02; n = 13 mice) with a temporal lag of 123 ± 9 ms (Fig. 2a–c), indicating that peaks in DA slightly precede dips in ACh. Importantly, DA and ACh showed a similar negative correlation outside of reward, whether mice were actively locomoting or remained immobile (Fig. 2a–c and Extended Data Figs. 4h and 5b–d). In agreement with this, we observed strong coherence between DA and ACh in the 0.5–4 Hz frequency band (Fig. 2d, e and Extended Data Fig. 5e, f) that maintained a phase offset of approximately 90 degrees (Fig. 2f–j and Extended Data Fig. 5g–k). By contrast, the mean amplitude of DA and ACh fluctuations differed between immobility, locomotion and reward, with DA and ACh transients being largest during reward and locomotion, respectively (Fig. 2h, i), despite considerable variability and overlap in the amplitude distribution of individual transients (Extended Data Fig. 3a, m, n). These data therefore show that DA and ACh transients maintain a consistent temporal relationship across behavioral states and suggest that rewards and movements do not create a unique sequence of neuromodulatory events in the striatum,

but instead recruit intrinsically-structured rhythms in DA and ACh that are also manifest during periods of rest.

DA-ACh coherence is strongest locally

To determine whether stereotyped coupling between DA and ACh extends to other striatal regions, we co-expressed and simultaneously imaged rDA1m and ACh3.0 in the DLS as well as in the dorsomedial striatum (DMS; Extended Data Fig. 6a). Within the DMS, extracellular DA and ACh levels were negatively correlated, fluctuated constantly and coherently at 0.5–4 Hz, and were consistently phase-shifted relative to one another irrespective of behavioral state (Extended Data Fig. 6b–j), showing that DA and ACh maintain a similar temporal relationship in the DMS as in the DLS. To determine if these fluctuations occur concurrently throughout the dorsal striatum, we compared DA transients in one striatal region to ACh signals in the other. DA and ACh transients between the DLS and the DMS were not coherent (Extended Data Fig. 6k, l), indicating that DA and ACh are not entrained by global brain-wide rhythms like breathing. Thus, although DA and ACh are stereotypically coupled locally, periodic fluctuations in the DLS are not synchronous with those in the DMS.

DA and ACh are not coordinated locally

Experiments in brain slices have convincingly demonstrated that DA release can briefly pause CIN firing via D2 receptors[24,25], while synchronous activation of CINs can evoke action potentials in DAN axons and cause widespread release of DA in the striatum following the activation of presynaptic β2-containing nicotinic ACh receptors (nAChRs) [20–23]. Thus, local coordination between DA and ACh may result from direct intra-striatal interactions between both neuromodulators. To investigate whether DA locally entrains ACh release *in vivo*, we simultaneously imaged DA and ACh in the DLS before and after locally infusing a control saline solution or a cocktail of DA receptor antagonists (n = 4 mice; Fig. 3a). Within a few minutes of infusion, the latter effectively prevented the rDA1m sensor from reporting spontaneous and reward-evoked changes in extracellular DA levels (Fig. 3b and Extended Data Fig. 7a), confirming our ability to block DA receptor signaling in the area imaged by our fiber optic. By contrast, this manipulation did not alter the timing or magnitude of spontaneous or reward-evoked ACh fluctuations compared to saline-infused mice (Fig. 3c, d and Extended Data Fig. 7b–d). To further test whether DA or other transmitters co-released by DANs (e.g., glutamate[29] or GABA[30]) entrain ACh, we imaged ACh3.0 in the DLS before and after lesioning midbrain DANs with either 6-OHDA (n = 7 mice) or viral expression of the pro-apoptotic enzyme Caspase-3 (n = 4 mice; Extended Data Fig. 7e, f). Spontaneous fluctuations in ACh persisted (Extended Data Fig. 7g, h), and even increased in amplitude and frequency in chronically-lesioned mice (Extended Data Fig. 7i, j), confirming that midbrain DANs are not required for striatal ACh levels to fluctuate periodically during immobility.

Next, we investigated whether ACh might directly entrain DA release within the striatum. We generated mice in which CINs cannot directly evoke axonal release of DA by conditionally deleting the β2 nAChR subunit specifically in DANs (Dat^{Cre};$\beta2^{floxed/floxed}$

mice; referred to as β2 cKO^{DAN}) and imaged rDA1m and ACh3.0 simultaneously in the DLS (Fig. 3e). β2 cKO^{DAN} mice (n = 6) showed intact DA and ACh responses to uncued rewards (Extended Data Fig. 8a, b), consistent with the well-established observation that reward-evoked DA release in the striatum derives from somatic bursting of DANs in the midbrain[3,4]. During immobility, DA and ACh transients were similarly unperturbed, fluctuating periodically at the same rate (Fig. 3f–h) and maintaining their strong coherence and phase relationship (Fig. 3i–l and Extended Data Fig. 8c–e).

To exclude the possibility that homeostatic adaptations occlude the influence that nAChRs normally exerts on DA terminals, we acutely blocked nAChR signaling in the DLS by locally infusing the antagonist DHβE (Extended Data Fig. 8f). Compared to mice treated with saline, DHβE (n = 8 mice) did not significantly affect reward-evoked responses nor spontaneous DA and ACh fluctuations (Fig. 3m and Extended Data Fig. 8g–j), or their coherence or phase relationship (Extended Data Fig. 8k), confirming that the strong coupling between DA and ACh is not dependent on striatal nAChR signaling *in vivo*.

ACh can also modulate DA release by activating muscarinic M5 receptors on DA axons[31]. Although this mechanism has not been implicated in ACh-evoked DA release[20–23], we examined its contribution by imaging DA and ACh following local infusion of the mAChR antagonist scopolamine in the DLS. As expected, this manipulation effectively blocked the detection of spontaneous and reward-evoked ACh transients by the ACh3.0 sensor (Extended Data Fig. 8l–n). By contrast, it did not affect reward-evoked DA release and only mildly diminished the power of spontaneous DA fluctuations in the 0.5–4 Hz band (Extended Data Fig. 8o, p), confirming the positive modulatory influence of mAChRs on DA release[31], and indicating that mAChRs are not required for producing periodic fluctuations in DA during immobility. Together, these data show that the periodicity and consistent temporal relationship between DA and ACh transients are not generated locally in the striatum via direct molecular interactions between both neuromodulators.

DA fluctuations arise in the midbrain

Our failure to reveal strong intra-striatal interactions between DA and ACh suggests that their coupling may instead be inherited from extra-striatal network dynamics. Previous studies indicate that phasic DA signals in the striatum arise from midbrain DANs, which fire coherently at 2–4 Hz[32–34] and integrate inputs distributed throughout the brain[35]. To determine whether intrinsic rhythms in striatal DA during immobility also originate in the midbrain, we expressed the genetically-encoded Ca^{2+} indicator GCaMP6f in midbrain DANs and simultaneously imaged somatodendritic Ca^{2+} signals in the SNc and axonal Ca^{2+} signals in the DLS using fiber photometry (Extended Data Fig. 9a). We observed a strong positive correlation between both signals during immobility (Extended Data Fig. 9b, c), suggesting that spontaneous fluctuations in striatal DA stem from the somatic activity of DANs in the midbrain. To causally test this, we infused the $GABA_A$ receptor agonist muscimol in the SNc while imaging rDA1m and ACh3.0 in the ipsilateral DLS using photometry (Extended Data Fig. 9d). Muscimol abolished spontaneous DA transients and strongly depressed global levels of DA in the DLS (Extended Data Fig. 9e, f), indicating that intrinsic fluctuations in striatal DA depend on the activity of midbrain DANs. Importantly,

inhibiting midbrain DANs with muscimol did not diminish spontaneous ACh fluctuations in the striatum (Extended Data Fig. 9e–h), confirming that sub-second transients in striatal DA and ACh are generated separately.

CIN coherence underlies ACh transients

Striatal CINs also fire coherently in response to reward and movement[5,6,19], but little is known about the factors that shape intrinsic ACh fluctuations during immobility. To reveal how periodic ACh transients emerge, we recorded the spiking activity of putative CINs (pCINs) from the DLS using high-density multi-shank silicon probes (Extended Data Fig. 10a). We distinguished pCINs, which make up approximately 2% of striatal neurons by established electrophysiological criteria, including spike waveform, firing rate and discharge properties (Extended Data Fig. 10b–g). pCINs were tonically active (firing rate: 5.7 ± 0.1 spikes per s; n = 150 pCINs from 51 recordings in 15 mice) and exhibited irregular, non-bursting firing (Fig. 4a). Importantly, their spikes tended to occur synchronously, with 91.7% of pairs of simultaneously recorded pCINs (n = 157 pairs) showing a significant peak in their spike cross-correlogram (CCG) at a lag of 0 s (Fig. 4a–c and Extended Data Fig. 10h, i). In addition, 30.6 % of pairs showed significant troughs at +0.25 and –0.25 s (Fig. 4c and Extended Data Fig. 10h, i), consistent with a 2 Hz rhythm.

To assess whether coordinated pCIN firing accounts for periodic fluctuations in extracellular ACh, we recorded the discharge of pCINs while simultaneously imaging ACh within overlapping regions of the DLS (Fig. 4d). We observed a clear relationship, where phasic increases in the firing of pCINs preceded peaks in ACh, while dips in ACh fluorescence followed coordinated decreases in pCIN firing (Fig. 4e, f and Extended Data Fig. 10j–p). In both cases, fluorescence lagged pCIN firing by ~100 ms, providing an independent estimate of the delay imposed by the ACh3.0 sensor kinetics (Extended Data Fig. 2). To determine whether the magnitude of ACh fluctuations correlates with the degree of spike coherence amongst pCINs, we compared spike-aligned ACh signals during different periods of network synchrony using the fraction of synchronously active pCINs as a proxy. Spikes occurring during periods of high coherence (i.e. when all recorded pCINs are synchronously active) were associated with large ACh transients that gradually declined in amplitude as coherence decreased (Fig. 4g, h). By contrast, spikes occurring in isolation (i.e. during periods of low network coherence) did not result in appreciable changes in extracellular ACh levels (Fig. 4g, h). Together, these data strongly suggest that coherent CIN firing drives periodic ACh fluctuations, the amplitude of which reflects the degree of local spike coherence amongst neighboring CINs.

Glutamate inputs drive ACh fluctuations

How does coherence amongst CINs arise? Striatal CINs receive convergent excitatory afferents from distributed cortical and thalamic regions[36], which can produce oscillations in the delta range (i.e. 1–4 Hz) in non-human primates and rodents during decision making and different states of arousal, including during quiet wakefulness[34,37,38]. We therefore postulated that synchronized glutamatergic inputs may coordinate CINs to produce periodic fluctuations in extracellular ACh levels. To test this, we imaged ACh while recording

striatal spiking activity and local field potential (LFP) oscillations, which largely reflect the activity of afferent inputs. ACh fluorescence was strongly modulated with respect to LFP oscillations in the 0.5–4 Hz frequency band (Fig. 4i, k), suggesting that coherence amongst CINs may be imparted by excitatory afferents. Indeed, the vast majority of pCINs recorded (94.6%) were significantly entrained to 0.5–4 Hz LFP oscillations with a preferred phase of 218 ± 6 degrees (Fig. 4j, k), consistent with negative LFP deflections reflecting an increase in excitatory drive onto pCINs. To further test whether glutamatergic inputs drive periodic ACh fluctuations, we delivered a cocktail of ionotropic glutamate receptor (iGluR) blockers locally in the DLS while imaging ACh3.0 and rDA1m (Fig. 4l). This treatment did not significantly decrease global ACh levels compared to saline, (Extended Data Fig. 9j), in line with the fact that CINs continue to fire cell-autonomously *in vivo* in the absence of glutamatergic drive[39]. By contrast, iGluR blockers reversibly depressed spontaneous ACh transients (Fig. 4m, n), but did not significantly depress intrinsic DA fluctuation or global DA levels (Fig. 4o and Extended Data Fig. 9k). Collectively, these data reveal that periodic fluctuations in DA and ACh are respectively driven by extra-striatal dopaminergic and glutamatergic inputs.

Discussion

It is commonly assumed that striatal circuits bathe in a steady concentration of DA and ACh provided by the tonic, cell-autonomous pacemaking of midbrain DANs and striatal CINs. This neuromodulatory ‘soup’ is occasionally interrupted by phasic increases or decreases in extracellular DA and ACh levels driven by sensory and motor stimuli that play important roles in reinforcement learning and motor performance[11,14,15]. Here, we show that these phasic signals are also prevalent when mice are immobile and in the absence of salient stimuli, with striatal DA and ACh levels fluctuating periodically at approximately 2 Hz. This observation, which hinges on the recent development of fast and specific sensors for DA and ACh with signal-to-noise sufficient to resolve single-trial responses calls into question the concept of a stable basal neuromodulatory tone in the striatum. Importantly, spontaneous changes in DA and ACh do not occur randomly: they are locally coherent at 0.5–4 Hz, with DA signals maintaining a 90-degree phase-shift relative to ACh across behavioral states. Thus, although the amplitude of DA and ACh fluctuations varies with behavior, ACh is unlikely to serve as a simple, context-specific gate or coincidence signal that disambiguates DA transients meant to promote learning versus movement[9,10]. In addition, this finding suggests that rewards and other salient stimuli do not create unique neuromodulator interactions in the striatum, but instead engage a common existing neural architecture that intrinsically supports rhythms in DA and ACh.

Surprisingly, the rapid, sub-second coordination between DA and ACh does not arise from mutual signaling between CINs and DA axons, despite strong evidence in brain slices that both modulators can directly interact with one another[20–25]. It is possible that CINs *in vivo* do not readily drive action potentials in DA axons given the propensity for nAChRs to desensitize in the sustained presence of ACh[40]. Another possibility is that DA and ACh release *in vivo* is not as synchronous as the electrical and optogenetic stimulations required to evoke DA release *ex vivo*[21–23]. Importantly, our data do not rule out more subtle intra-striatal interactions between DA and ACh that are context-dependent[20], that take

place on subcellular scales not resolved by photometry or that develop on time courses slower than those investigated here. Indeed, the reinforcing properties of nicotine depend on nAChR signaling onto midbrain DANs[41], and prolonged changes in DA receptor signaling are known to alter the electrophysiological properties of striatal CINs[6,42].

Our data instead support a model where spontaneous rhythms in striatal DA and ACh are inherited from extra-striatal afferents. Fluctuations in striatal DA reflect the somatic activity of dopaminergic inputs from the ventral midbrain, while ACh transients are driven by glutamatergic afferents acting to synchronize the discharge of neighboring CINs. Excitatory inputs from the cortex and thalamus are sufficient to drive phasic elevations in ACh[43] and may contribute to pauses in CIN firing via feed-forward inhibition or periodic withdrawal of excitatory drive[44]. Importantly, the magnitude of ACh fluctuations correlates with the degree of population synchrony amongst CINs, which increases when the brain produces concerted movements[19] or responds to salient sensory stimuli[6]. Striatal ACh levels may therefore be construed as a moment-to-moment measure of coherence in the activity of distributed cortico- and thalamo-striatal afferents. Midbrain DANs similarly integrate excitatory (and inhibitory) inputs from many brain areas[35], exhibit significant baseline correlations in spiking that increase in strength upon reward presentation and learning[32], and their coherent discharge accounts for phasic changes in striatal DA levels more so than bursting of individual neurons[33]. Thus, DA and ACh both reflect the concerted dynamics of widely distributed neural circuits[45]. How DA rhythms coordinate with ACh rhythms in the DLS and in other striatal regions, including in the ventral striatum, remains an important question for future investigations, but a fascinating possibility is that midbrain DANs and striatal CINs innervating contiguous striatal regions are embedded in parallel cortico–basal ganglia–thalamo–cortical loops and sample common inputs oscillating in the 0.5–4 Hz range[34,37,38].

Together, our data provide a novel framework for understanding how the basal ganglia motivate and reinforce behavior. First, the fact that DA and ACh levels fluctuate constantly indicates that the net effect of one modulator on striatal circuits cannot be fully understood without taking into consideration the other, as the striatum is composed of multiple populations of cells expressing G protein-coupled receptors for both modulators that engage distinct (and sometimes antagonistic) intracellular signaling cascades. Second, the presence of spontaneous reward-like rhythms in DA and ACh suggests that the established functions of both modulators in learning and synaptic plasticity extend beyond the time of reward delivery. Indeed, learning, decisions and actions are not exclusively driven by external rewards and salient sensory stimuli. Third, the phase offset between DA and ACh may create temporally-defined windows for learning, such that synaptic plasticity may preferentially occur when direct- and indirect-pathway SPNs fire within specific phases of this endogenous rhythm[12,13,46], with repeated reactivation of SPN ensembles during post-learning rest offering a potential solution to the credit assignment problem[47]. Lastly, intrinsic fluctuations in DA and ACh may help specify the timing of self-paced volitional actions[7,14,15,19] as well as sustain cognitive processes that lack overt behavioral correlates[48–50]. Thus, the autonomously-coordinated rhythms in DA and ACh revealed here provide a lens through which to understand the structure of activity within the basal ganglia as well as its impact on behavior in health and in neuropsychiatric disorders.

Methods

Ethical compliance

All experimental procedures were performed in accordance with protocols approved by the NYU Langone Health (NYULH) Institutional Animal Care and Use Committee (protocol number IA16–02082) and in compliance with the Guide for Animal Care and Use of Laboratory Animals.

Animals

Mice were housed in group before surgery and singly after surgery under standard laboratory conditions (70 ± 2°C; 50 ± 10% humidity; reverse 12-hour light-dark cycle, with dark from 10 a.m. to 10 p.m.) with *ad libitum* access to food and water, except when water-restricted to incite consumption of water rewards. For conditional deletion of choline acetyl-transferase (ChAT) from forebrain cholinergic interneurons, a floxed ChAT line was crossed with *Nkx2.1*^{Cre} transgenic mice (both kindly provided by Dr. Robert Machold, NYULH), as described previously[51]. For conditional deletion of the β2 nAChR subunit from dopamine neurons, a floxed β2 line[52] (kindly provided by Dr. Michael Crair, Yale) was crossed with *Dat*^{Cre} knockin mice[53] (Jackson Laboratory strain #006660). C57BL6/J mice were used as control animals (Jackson Laboratory strain #000664). Experiments were carried out using both male and female mice at 8–24 weeks of age (for fiber photometry experiments, 54% of animals used were female; for electrophysiology experiments, 50% of animals used were female); we did not observe significant differences between females and males (Extended Data Fig. 3o, p) and therefore used combined data for analyses.

Stereotaxic surgery

Mice were anaesthetized with isoflurane, placed in a stereotaxic apparatus (Kopf Instruments) on a heating blanket (Harvard Apparatus) and administered Ketoprofen (10 mg/kg, subcutaneous). The scalp was shaved and cleaned with ethanol and iodine solutions before exposing the skull. For simultaneous recordings of dopamine (DA) and acetylcholine (ACh) in the dorsolateral striatum (DLS), craniotomies were drilled above the injection site (from bregma, in mm: AP +0.5, ML +2.5 for 0° angle implants or AP +0.5, ML +3.25 for 30° angle implants). 200 nL of a 1:1 mix of AAV9-hSyn-ACh3.0 (titer: 1.46 e+13; Vigene Biosciences) and AAV9-hSyn-rDA1m (titer: 1.91 e+13; Vigene Biosciences) was injected 2.0 mm below dura (0° angle) or 1.6 mm below dura (30° angle) at a rate of 100 nL/min using a microsyringe pump (KD Scientific; Legato 111) fitted with a Hamilton syringe (1701N, gastight 10 μL) connected to a pulled glass injection micropipette (100 μm tip; Drummond Wiretrol II) via PE tubing filled with mineral oil. Injection micropipettes were left in place for 5 min before removal. The optimal dilution of each AAV was empirically determined to enable strong expression while avoiding toxicity. Fiber optics (400 μm diameter; NA = 0.5) were either custom-made (Thorlabs FP400URT fiber optic connected to Thorlabs CFLC440 ceramic ferrule) or purchased from RWD Life Science (R-FOC-BL400C-50NA). Fibers were implanted above the injection site to and cemented to the skull using C&B metabond (Parkell). Only fibers with greater than 75% transmission efficiency were selected for surgical implantation. For mice used for simultaneous recording of ACh and DA in DLS and ipsilateral DMS, additional craniotomies were drilled above the

DMS injection site (from bregma, in mm: AP +0.7, ML +1.3 for −5° angle implants). 200 nL of a 1:1 mix of AAV9-hSyn-ACh3.0 and AAV9-hSyn-rDA1m was injected 2.0mm below dura and a second optic fiber was implanted at a depth of 1.85mm below dura.

For simultaneous recording of GCaMP6f[54] signal in the DLS and SNc, a craniotomy was drilled above the SNc (from bregma, in mm: AP −3.14, ML +1.42) in *Dat*^{Cre} knockin mice. 400 nL of AAV1-hSyn-FLEX-GCaMP6f (titer: 4.38 e+13; Penn Vector Core) was injected at a depth of 4.0 mm below dura at a rate of 100 nL/min. A fiber optic cannula was implanted above the injection site and a second fiber optic cannula was implanted above the DLS (from bregma, in mm: AP +0.5, ML +2.5, at a depth of 2.0 mm); both were cemented to the skull using C&B metabond.

For mice used for acute intra-striatal pharmacological infusions in the DLS, a custom guide cannula (Plastics One; 26 gauge) was chronically implanted ipsilateral to the chronic optic fiber implant at AP +0.5 and ML +1.7 at a −10° angle at a depth of 1.75 mm below the pial surface. For mice used for acute pharmacological infusions in SNc, custom guide cannula was chronically implanted at AP −3.14 and ML +1.42 at a depth of 4.0 mm below the pial surface, posterior to the chronic optic fiber implanted in the DLS, as above. Guide cannulas were cemented to the skull using C&B metabond and covered with dummy cannulas. All mice had a custom titanium headpost implanted over lambda using C&B metabond to allow head fixation during recordings. Mice were allowed to recover in their cage for two weeks before head-fixation habituation, treadmill and lick spout training, and recordings.

For mice used for acute electrophysiological recordings in the DLS, a second surgery was performed after the post-recover period, head-fixation habituation, and treadmill training. Mice were head-fixed using the previously cemented titanium headpost. A craniotomy centered on ML +2.0 mm and extending from AP −0.5 mm to +1.5 mm was drilled and dura was carefully removed 24 h prior to recording. For acute electrophysiological recordings in the dorsomedial striatum (DMS), the craniotomy was centered on ML +1.0 mm. A second craniotomy (AP −1.0 mm, ML −1.0 mm) was drilled for grounding during recordings. Both craniotomies were covered with silicone sealant (Kwik-Cast) until recording. After craniotomies, mice were allowed to recover in their cage for one day before recordings.

For experiments evaluating the effects of DA neuron loss on entrainment of ACh release, an additional stereotaxic surgery was performed under isoflurane anesthesia after baseline imaging sessions. Desipramine (25 mg/kg) and pargyline (5 mg/kg) were administered intraperitoneally prior to surgery to increase the selectivity and efficacy of 6-hydroxydopamine (6OHDA) lesions[55]. A small craniotomy was performed above the substantia nigra pars compacta ipsilateral to the imaged striatum (AP −3.1 mm, ML +1.3 mm, marked during first stereotaxic surgery) and 3 μg of 6-OHDA (total volume: 200 nL) was injected 4.2 mm below dura at a rate of 100 nL/min. Alternatively, DA neurons were lesioned using AAV-mediated expression of Cre-dependent Caspase-3[56] in midbrain DA neurons of *Dat*^{Cre} mice. To do so, four craniotomies were performed above the SNc ipsilateral to the imaged striatum (in mm: AP −2.9, ML +0.6; AP −2.9, ML +1.25; AP −3.4, ML +0.6; AP −3.4, ML +1.25; all marked during first stereotaxic surgery) and 300 nL of AAV1-EF1a-FLEX-taCasp3-TEVp (titer 2.8 e+13; UNC Vector Core) was injected at each

site 3.8–4.1 mm below dura at a rate of 100 nL/min. All mice were allowed to recover in their cage for two weeks, with once daily subcutaneous injections of ketoprofen (10 mg/kg in 0.9% saline) for the first three post-operative days.

Behavior Analysis

Mice were habituated to head-fixation in the rig in a dark soundproof chamber and locomotion on a transparent cylindrical wheel[57] for a minimum of 5 days prior to any recording. A subset of mice had access to water within their home cage restricted to incite consumption of water delivered from a spout at semi-random intervals during imaging sessions. Licking was monitored using a capacitive touch sensor (Sparkfun AT42QT1010). Solenoid valve (Lee Company LHQA0531220H) opening and lick sensor signals were acquired using Wavesurfer as digital inputs to a National Instruments data acquisition board (PCIe-6353) and breakout terminal block (BNC-2090A) at a sampling rate matching the photometry signal acquisition rate. Reward delivery and lick event times were recorded as time points exceeding a threshold of 0.5 V. Analyses and figures of reward-evoked DA and ACh transients were limited to solenoid openings without detected licks in the preceding 0.2 s and with consummatory licks detected within 1 s of solenoid valve opening, unless specified otherwise. On average, the first lick occurred within 164 ± 12 ms of solenoid opening.

Treadmill velocity was extracted from positional information provided by a rotary encoder (MA3 magnetic shaft encoder, US Digital), down-sampled to 50 Hz for all recordings. Immobility was defined as any period of time lasting at least 4 s during which velocity does not exceed 0.25 cm/s beginning at minimum 0.5 s after treadmill velocity decreases below 0.25 cm/s and ending 1 s before treadmill velocity exceeds 0.25 cm/s again. Solenoid openings, licking responses and postural adjustments on the wheel (e.g. grooming, detected using an infrared camera (Sony AKK CA20 2.8 mm FPV camera) were excluded from periods of immobility. Movement bouts were defined as any period of time when absolute treadmill velocity exceeded 4 cm/s for a minimum of 4 s, preceded and followed by 4 s of immobility. Treadmill acceleration was calculated as the first derivative of smoothed (*movmean* function in MATLAB; window, 0.2 s) treadmill velocity. Peaks of positive acceleration were determined by finding the time points of local maxima (*findpeaks* function in MATLAB with optimized thresholds, minimal prominence: 0.5 cm/s^2) during periods of active locomotion.

Open field experiments were conducted in a 30 × 30 cm arena with clear plexiglass floor and walls cleaned thoroughly between trials. Mice were habituated to the arena for 30 min per day for a minimum of 5 days prior to recording. On the day of recording, individual animals were placed in the arena for 30 min while a camera (Basler; acA2000–165um NIR) placed 20 inches below the center of the arena captured frames at 30–60 Hz. Each frame's time stamp was acquired using Wavesurfer to allow for alignment to simultaneously-recorded photometry data. Periods of immobility and locomotion were isolated using EthoVision XT 11.5 software (Noldus) whenever the center of mass of the mouse remained below 0.25 cm/s or exceeded 4 cm/s, respectively, for a minimum of 4 consecutive seconds.

Fiber Photometry Recording

To excite the GRAB sensors ACh3.0 and rDA1m, we used fiber-coupled LEDs at 470 nm (Thorlabs M470F3) and 565 nm (Thorlabs M565F3), respectively. Excitation light was passed through a fiberoptic patch cord (Doric 400 μm 0.48 NA) to a fluorescence mini-cube (Doric FMC5_E1(460–490)_F1(500–540)_E2(555–570)_F2(580–680)_S) and connected to the chronic optic fiber implant in the mouse via a fiberoptic patch cord (Doric 400 μm 0.48 NA). Emission light was collected through the same patch cord and fluorescence mini-cube connected to two photoreceivers (Newport 2151, set to DC mode) using a fiberoptic patch cord (Doric 600 μm 0.48 NA); one for green emitted light, and another for red emitted light. Excitation light was delivered in one of two modes: continuous wave (CW) or frequency modulated (FM). We used the former to image mice expressing a single sensor and when performing concurrent *in vivo* extracellular recordings to minimize opto-electric artefacts. FM mode was used for imaging DA and ACh sensors simultaneously to minimize cross-talk between fluorescence channels. In CW mode, light power measured (Thorlabs PM100D) at the tip of fiber optic patch cord was set to 20–60 μW by manually adjusting the LED driver before each recording. In FM mode, a sinusoid generated using Wavesurfer software (Janelia) and outputted from a National Instruments data acquisition board (PCIe-6353) and breakout terminal block (BNC-2090A) was used to drive the fiber-coupled LED. The 473 nm and 565 nm LEDs were modulated at either 217 Hz or 319 Hz, alternating between recording sessions. Light power was set by adjusting amplitude and offset parameters of the sinusoidal control voltage by monitoring the output voltage from the photoreceiver using Wavesurfer software to achieve a sinusoid peak-to-peak amplitude of 1–2V. After each recording session, light power (18–62 μW) was measured at the tip of the fiberoptic patch cord. We ensured that imaging in FM mode does not generate artefactual oscillations by repeating key observations in mice with only one fluorescent sensor expressed at a time in CW mode. Photometry signals read out by the photoreceiver were digitized at 2 kHz (for CW mode) or 5 kHz (for FM mode) by a National Instruments acquisition board (NI BNC-2090A) or at 30 kHz (for combined fiber photometry and acute electrophysiology recordings) by an Open Ephys acquisition board.

Acute Electrophysiological Recording

Electrophysiological recordings were made with silicon microprobes[58] (128D; IDAX microelectronics) affixed to metal rods acutely lowered into the brain using a micromanipulator (Scientifica PatchStar). For DLS recordings, probes were inserted perpendicularly to brain surface at approximately AP +0.0 to +1.0 mm and ML +2.0 or +2.5 mm to a depth of about 2.5–3.0 mm. Prior to insertion on each recording day, the electrode shafts were coated with fluorescent dye (DiI, Thermo Fisher Scientific V22885) for *post-hoc* identification of probe insertion location. Probes were lowered at a speed of 1 μm/s to limit tissue damage and, once at the desired depth, were left in place for at least 45 min prior to initiating a recording to allow for the tissue to settle and minimize unit drift. Electrophysiological data were recorded with Open Ephys at a sampling rate of 30 kHz. Wheel positional encoder and, when applicable, photometry data were also recorded using an I/O board connected to the Open Ephys acquisition board at a sampling rate of 30 kHz.

Fiber Photometry Analysis

Photometry signal processing. Raw photometry signals collected as a voltage from the photoreceiver were processed using custom MATLAB code. For recordings in CW mode, raw voltage signals were first low-pass filtered at 20 Hz using a Butterworth filter to remove high-frequency noise. The filtered signal was then down sampled to 50 Hz (above the Nyquist frequency to prevent aliasing), and the final photometry signal (outputted as a % value) was obtained using the equation $\Delta F/F = (F - F_0)/F_0$, in which F_0 is baseline fluorescence. The latter was computed by interpolating the bottom percentile of fluorescence values measured in 10 s-long sliding windows (0% overlap) along the entire photometry trace. For recordings acquired in FM mode, a copy of each sinusoid generated in Wavesurfer was recorded as a reference signal alongside the modulated green and red fluorescence signals from the photoreceivers. We demodulated fluorescence signals as follows: First, each fluorescence signal was band-pass filtered (reference sinusoid frequency ± 10 Hz; Butterworth; order: 6) to isolate the main frequency component. Next, we determined whether the reference and fluorescence sinusoids were in-phase or out-of-phase. If in-phase, we performed a phase-dependent demodulation by a) subtracting the mean of the reference and fluorescence sinusoids to remove any DC offset, b) multiplying the reference and fluorescence sinusoids, and c) low-pass filtering (20 Hz) the resulting signal to extract the demodulated fluorescence. More commonly however, the reference and fluorescence sinusoids were slightly out-of-phase. In this case, we used a standard quadrature demodulation method (which calls for phase-shifting the reference signal by 90 before multiplying it to the fluorescence sinusoid, and then low-pass filtering the resulting signal at 20 Hz) to demodulate the fluorescence signal (see refs. [59, 60]). The demodulated fluorescence traces were finally down-sampled to 50 Hz and baseline-adjusted as described above.

Frequency analysis.—Analysis of frequency components enriched in the ACh and DA photometry signals was performed on raw, unfiltered, non-demodulated, non-downsampled fluorescence signals from time periods when mice were immobile (unless specified otherwise). We computed the fast Fourier transform of these data using the *fft* function in MATLAB and extracted the single-sided amplitude (power) spectrum across frequency domains spanning 0 to 0.5*acquisition sampling frequency. Power spectra shown in Fig. 1i and 1m were normalized by subtracting the power at 100 Hz and dividing by the power at 0.1 Hz. To isolate power specifically contributed by DA and ACh in Fig. 1j and 1n (and in all similar figures subsequently), we then subtracted the mean normalized power spectrum of the inert fluorophores tdTomato and GFP, respectively, across the same frequency domains. To compare DA and ACh power statistically across mice and conditions (as in Fig. 1k and 1o, and in similar figures subsequently) we computed the area under the curve (AUC) of power spectra within the 0.5–4 Hz frequency band.

Cross-correlation analysis.—To correlate ACh3.0 and rDA1m fluorescence, we calculated the Pearson cross-correlation coefficient *r* between the two photometry signals using the *xcorr* function in MATLAB (window, 1 s; bin, 20 ms) after parsing them based on behavioral state (i.e. reward, locomotion, or immobility). Confidence intervals were computed by repeatedly calculating Pearson's *r* after one of the photometry signals was

shifted in time (increment, 1 s; repeats, 100) and then extracting the 2.5th and 97.5th percentiles across the correlation window for each bin to generate a 95% confidence interval. The correlation coefficient *r* and lag at the maximal absolute deflection were computed and compared across behavioral states and/or cohorts, as shown in Fig. 2b and 2c. We applied the same process to correlate ACh or DA fluorescence and wheel acceleration, as shown in Extended Data Fig. 4h, and to correlate GCaMP6f fluorescence imaged in the DLS and SNc, as shown in Extended Data Fig. 9c.

Coherence analysis.—To quantify how closely DA and ACh fluorescence signals co-vary in time and the relative timing between the two signals, we computed their coherence and extracted the magnitude of the coherence and phase offset, respectively. We performed this over different frequency domains to examine in which frequency band coherence is greatest, as well as over time domains to examine whether the degree of coherence and phase offset between DA and ACh varied between behavioral states. We computed coherence using a custom MATLAB script adapted from code acquired from the Buzsaki lab[61] (https://github.com/buzsakilab/buzcode). Briefly, we calculated the magnitude and phase of the DA–ACh coherogram using a multi-taper estimation with the chronux function *cohgramc* (window, 10 s; overlap, 5 s; step, 5; padding, 0). We computed confidence intervals by randomly shifting one of the photometry signals (increment, 1 s; repeats, 100) and extracting the 2.5th and 97.5th percentiles of the magnitude and phase of the resultant coherogram for each repetition to generate a 95% confidence interval. To compare coherence at different frequencies, we averaged coherence magnitude and phase offset across the time dimension, as shown in Fig. 2d and 2f and in other similar figures. To compare each between behavioral states, we calculated the median coherence magnitude and phase offset within the 0.5–4 Hz frequency band, as shown in Fig. 2e and 2g and in others like it. Phase offset was only examined if a significant effect of coherence magnitude was observed.

Phase analysis.—To estimate instantaneous phase across time, each photometry signal was filtered (0.5–4 Hz; Butterworth; order: 3) and the phase angle of the Hilbert transform was extracted using the *hilbert* function in MATLAB. We next extracted the amplitude of the DA and ACh fluorescence signals corresponding to each oscillatory cycle (from –180 to +180 degrees; bin size: 10 degrees) and calculated the mean amplitude within each bin. To highlight the temporal relationship between DA and ACh across behavioral states, we normalized fluorescence amplitude between 0 to 1 across each full cycle, as shown in Fig. 2j and in others like it. We applied the same process to determine the relationship between the phase of ACh or DA fluctuations and wheel acceleration, as shown in Extended Data Fig. 4i–j.

Pharmacological infusions analysis.—The effects on ACh and DA fluctuations by intra-striatal drug infusions were assessed by comparing photometry signals immediately preceding and following completion of drug infusion, unless specified otherwise. To measure relative changes in the overall extracellular concentration of DA or ACh in the striatum, we first estimated the fraction of the voltage recorded by the photoreceiver that specifically reflects extracellular neurotransmitter levels (vs. that contributed by auto-

fluorescence of the brain and photometry system). We term this metric 'global DA or ACh levels' and normalized its dynamic range such that a value of 1 reflects the fluorescence attributed to extracellular DA or ACh under baseline recording conditions and a value of 0 the fluorescence in the presence of pharmacological antagonists for either sensor (D1/2R antagonist for rDA1m and mAChR antagonist for ACh3.0; see Extended Data Figs. 9f, i–k). We expressed changes in global DA or ACh levels caused by intra-striatal infusions of pharmacological antagonists by normalizing post-infusion fluorescence to pre-infusion levels.

Acute Electrophysiological Analysis

Spike sorting and putative cell type determination.—Raw electrophysiological data was spike-sorted using Kilosort 2 (www.github.com/MouseLand/Kilosort2) and the resulting spike clusters were visualized and manually curated using Phy2 (https://phy.readthedocs.io/en/latest). High-quality single units were identified based on the following inclusion criteria: (1) waveform trough to peak amplitude exceeding 80 μV; (2) a minimum of 500 spikes recorded per 5400 s recording session; (3) waveform peaks preceding waveform troughs; (4) presence of a clear refractory period, assessed by considering the length of time that the firing rate of a unit is suppressed following a spike in auto-correlograms (window, 1 s; bin, 1 ms). Units passing these quality criteria were then classified into three putative striatal cell types: putative striatal projection neurons (pSPNs), putative cholinergic interneurons (pCINs), and a third class of unidentified neurons (others, which likely includes fast-spiking interneurons and other GABAergic interneurons) using established criteria[62–67] such as firing rate, coefficient of variation, phasic activity index, and spike waveform duration. The firing rate of a unit was calculated as the number of spikes divided by the duration of the recording. The coefficient of variation (CV) was defined as the standard deviation of the distribution of inter-spike intervals (ISIs) divided by the mean of the distribution. The index of phasic activity was calculated as the fraction of recording time containing ISIs longer than two seconds. The waveform duration was calculated as the time between the maximum downward spike deflection to the following upward peak. For analyses during immobility or locomotion, we extracted spikes that occurred during windows of time when the animal was determined to be immobile or actively locomoting, respectively, using criteria described in *Behavior Analysis* above.

Spike train cross-correlation.—In recordings with ≥ 2 simultaneously recorded pCINs, we first generated pairs using the *nchoosek* function in MATLAB. For each pair of pCINs, one was randomly selected to be the reference unit and we calculated the spike cross-correlogram (CCG) for that pair as a count of the number of spikes emitted by one pCIN relative to the spikes of the reference unit (window, 2 s; bin, 10 ms). We normalized spike counts to a firing rate by dividing by number of spikes within each time bin by the total number of reference unit spikes and by bin size: firing rate = (spike counts/n_{ref})/bin duration (s). To allow comparisons across units with different baseline firing rates, we mean-normalized instantaneous firing rates by subtracting the mean firing rate (μ) of the non-reference unit during a given behavioral state before dividing the resultant value by the same mean: Normalized instantaneous rate = (instantaneous rate – μ)/μ. To compute confidence intervals, we ran a CCG using the same reference unit and a shuffled spike train

of the second pCIN. Each shuffled spike train was generated following random permutations of a unit's inter-spike intervals before computing the 2.5th and 97.5th percentiles of the resulting shuffled CCGs. Lastly, to assess the proportion of units that significantly increase their firing rate, we identified all the time bins at various lags where the CCG output was either above or below the 95% confidence interval.

Firing rate change at event times.—For recordings where ACh fluorescence was imaged concurrently with spiking activity, we determined the instantaneous firing rate of pCINs relative to peaks and troughs in ACh by filtering photometry signals (0.5–4 Hz; Butterworth; order: 3), identifying transients larger than 2 standard deviations from the filtered signal, and computing a peri-event time histogram by aligning spike times to event times such as ACh peaks and ACh troughs. Spike times were counted in 20 ms bins (determined based on the final sampling rate of the photometry signal, 50 Hz) across a two second time window centered on the event times, and then averaged across all events to generate a rate. We normalized firing rate change at event times to the mean firing rate for a given behavioral state to allow for comparison between units of different firing rates. To obtain a 95% confidence intervals, a shuffled spike train (maintaining the same distribution of inter-spike intervals) was instead aligned to event times. To assess the proportion of units that significantly change their firing rate, we determined the number of bins where a unit's firing rate either exceeds or falls below the 95% confidence interval.

Coherent spiking analysis.—Only recordings with ≥ 2 pCINs and concurrent imaging of ACh fluorescence were included. Spike trains were first parsed to include only spikes occurring during immobility, as defined in Behavioral Analysis. For each spike of a selected reference pCIN, we determined if other pCINs discharged within ± 10 ms by generating peri-event counts relative to spikes. The resulting output was a matrix of binary values, with the number of columns reflecting the length of the spike train of the reference unit and the number of rows corresponding to the number of concurrently recorded units (n). This output matrix was then summed across all rows, such that the range of values of the final vector would be 1 to n. Lastly, spike times of the reference unit were stratified based on the value within each bin. Bins where only 1 out of n units spiked reflect low synchrony amongst the population of pCINs, whereas bins with a value of N out of N possible units corresponded to synchronous activity across all concurrently recorded pCINs. Simultaneously recorded ACh photometry signal was aligned to stratified spike times of the reference unit, and a spike-triggered average was computed by averaging the photometry signal across each group (1/n to n/n), as shown in Fig. 4g. To compare units across multiple recordings with a variable total number of pCINs, only 1/n and n/n spike-triggered averages were used, as shown in Fig. 4h. For computation of a 95% confidence intervals, the simultaneously recorded photometry signal was aligned to spike times in a shuffled spike train (maintaining the same distribution of inter-spike intervals) and the 2.5th and 97.5th percentiles were extracted across spike-triggered averages.

LFP analysis.—Local field potential (LFP) signals were extracted from wideband electrophysiological recordings from one striatal channel and down-sampled to 1250 Hz. The LFP was then filtered at 0.5–4 Hz and the instantaneous phase was determined using

a Hilbert transform. Phase locking was determined by calculating the instantaneous phase angle at each spike time for a given unit during immobility. A histogram of phase angles was calculated, and the circular mean and resultant vector was calculated for each unit, as shown in Fig. 4j. Only units that were significantly modulated (Rayleigh test) were included in the analysis. For recordings where ACh fluorescence was imaged concurrently, phase-locking was determined by calculating a histogram of photometry signal amplitudes at each phase angle, and rescaling across each cycle, as shown in Fig. 4i. Cross-correlation between the filtered LFP signal and concurrently recorded photometry signal and was calculated as above.

Histology

Mice were deeply anesthetized with isoflurane and perfused transcardially with 4 % paraformaldehyde in 0.1 M sodium phosphate buffer. Brains were post-fixed for 1–3 days and sectioned coronally (50–100 μm in thickness) using a vibratome (Leica; VT1000S). ACh3.0 and rDA1m were either imaged directly (i.e. endogenous fluorescence; as in Fig. 4d and Extended Data Fig. 1a) or after immunofluorescence staining (see Extended Data Figs. 1b–d, 7h) by incubating free-floating sections with chicken anti-GFP (Abcam ab13970; 1:2000) and rabbit anti-DsRed (Takara 632496; 1:1000) polyclonal antibodies overnight at 4°C. DA axons in Extended Data Fig. 7h were labeled using a rat anti-DAT monoclonal antibody (Sigma MAB369; 1:1000). The following secondary antibodies (all from Thermo Fisher Scientific) were applied for 2 hours at room temperature: goat anti-chicken Alexa Fluor 488 (A-11039; 1:1000), goat anti-rabbit Alexa Fluor 568 (A-11036; 1:1000) and goat anti-rat Alexa Fluor 647 (A-21247; 1:1000). Brain sections were subsequently mounted on superfrost slides and cover slipped with ProLong antifade reagent with DAPI (Molecular Probes). Low-magnifications images of whole sections were obtained with an Olympus VS120 slide scanning microscope, while high-magnification optical sections were imaged using a Zeiss LSM 800 Airyscan confocal microscope.

Reagents

Drugs (all from Tocris) were reconstituted and stored according to the manufacturers' recommendations. For systemic antagonism of mAChRs and D2Rs in Fig. 1h–o, scopolamine (2 mg/kg) and sulpiride (30 mg/kg) were prepared daily in sterile physiological saline (0.9% NaCl) and administered intraperitoneally 30 min prior to the start of photometry recordings. For local injections within the DLS, an internal cannula (Plastic One; 33-gauge) was connected to a syringe (Hamilton; 1701N, gastight 10 μL) through a tube containing either HEPES-buffered sterile saline or a pharmacological agent dissolved in saline, and was inserted into the guide cannula before the recording session. Drug infusion controlled by a microsyringe pump (KD Scientific; Legato 111; rate: 50–100 nL/min) was initiated 10–20 min after baseline recording. The following drugs were used: 1 mM NBQX (2,3-Dioxo-6-nitro-1,2,3,4-tetrahydrobenzo[*f*]quinoxaline-7-sulfonamide) and 5 mM D-AP5 (D-(−)-2-Amino-5-phosphonopentanoic acid) to block iGluRs, 0.4 mM SCH23390 to block D1Rs, 0.6 mM sulpiride to block D2Rs, 5 mM DHβE (dihydro-β-erythroidine hydrobromide) to block nAChRs and 1 mM scopolamine to block mAChRs. To estimate the extent of drug infusion in the striatum in Fig. 3a, drugs were substituted with Alexa Fluor 594 hydrazide (Invitrogen, A10442). To inhibit neural activity in the ventral midbrain in

Extended Data Fig. 9d–h, 1 mM muscimol dissolved in HEPES-buffered sterile saline was infused at a rate of 50 nL/min into the SNc.

Statistics

The experiments were not randomized, as comparisons were either made within subject (e.g., saline vs. antagonist infusions in the same animal) or between mice of different genotypes (e.g., control vs. β2 cKO^{DAN} mice). Data were not acquired blind to experimental condition, but were subjected to identical analyses and compared statistically in MATLAB using the following tests (as indicated in the text): Student's paired two-sided *t*-test for comparisons between paired data points, Student's two-sample two-sided *t*-test for comparisons between un-paired data points, and one-way balanced analysis of variance (ANOVA) followed by Dunn's Multiple Comparison Test for comparisons between multiple groups. For fiber photometry experiments, n-values represent the number of mice. All imaging sessions obtained per condition from the same mouse (average: 2 sessions per condition per mouse; range: 1–4) were concatenated and analyzed as n = 1. For electrophysiology recordings, n represents the number of units or unit pairs. Histological analyses were independently replicated in at minimum 3 mice. No statistical methods were used to predetermine sample size. Data are reported in text and figures as mean ± standard error of mean (s.e.m.), with shaded areas and error bars in figures representing s.e.m. Exact p-values are provided in text and figure legends, and statistical significance in figures is presented as * $p < 0.05$, ** $p < 0.01$ and *** $p < 0.001$.

Extended Data

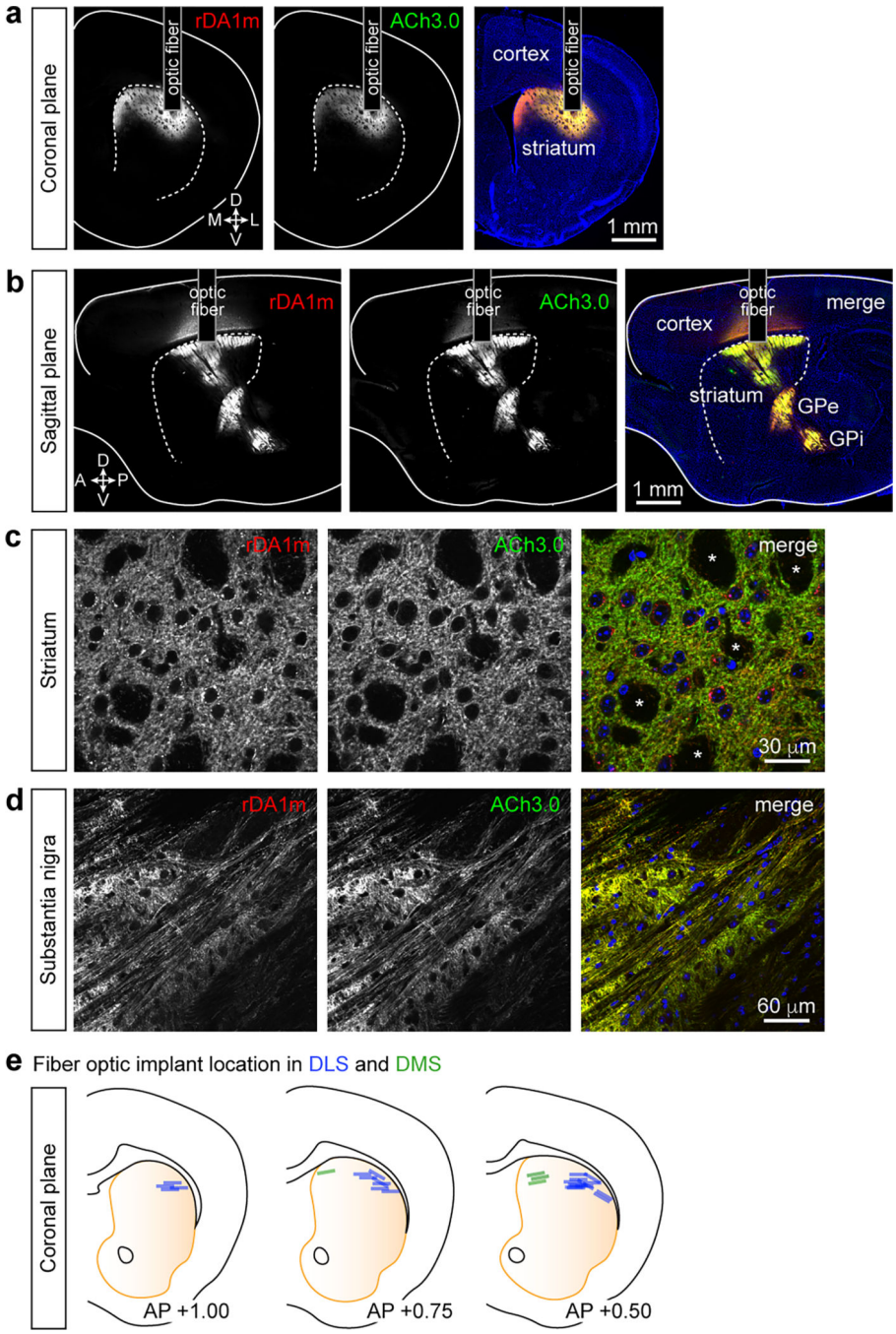

Extended Data Fig. 1. Characterization of rDA1m and ACh3.0 expression.

a, Epifluorescence images of endogenous rDA1m (*left*) and ACh3.0 (*middle*) fluorescence in a coronal section of the striatum. *Right*, merged image overlaid with DAPI nuclear stain (blue). Similar results were obtained in n = 16 other brains recovered for post-hoc validation of GRAB sensor expression and fiber optic placement. **b**, Epifluorescence images of immuno-enhanced rDA1m and ACh3.0 expressed in the dorsal striatum. Note the presence

of rDA1m- and ACh3.0-positive axonal projections in the globus pallidus externus (GPe) and internus (GPi), consistent with the subcellular distribution of dopamine and muscarinic receptors in both direct and indirect-pathway SPNs. **c**, High magnification confocal images (single optical plane) of immuno-enhanced rDA1m and ACh3.0 in a coronal striatal section. Note the localization of both sensors to the somatic membranes of striatal neurons and throughout the neuropil, and their exclusion from corticofugal axon bundles (asterisks). Note also that some rDA1m forms intracellular aggregates. **d**, Same as **c** for a sagittal section of the substantia nigra pars reticulata. Subcellular localization of immuno-enhanced rDA1m and ACh3.0 by high magnification confocal microscopy was independently confirmed in four mice. **e**, Schematic showing the tip of all recovered fiber optic implants in the DLS (blue) and DMS (green) at 3 different anterior-posterior levels relative to bregma (in mm).

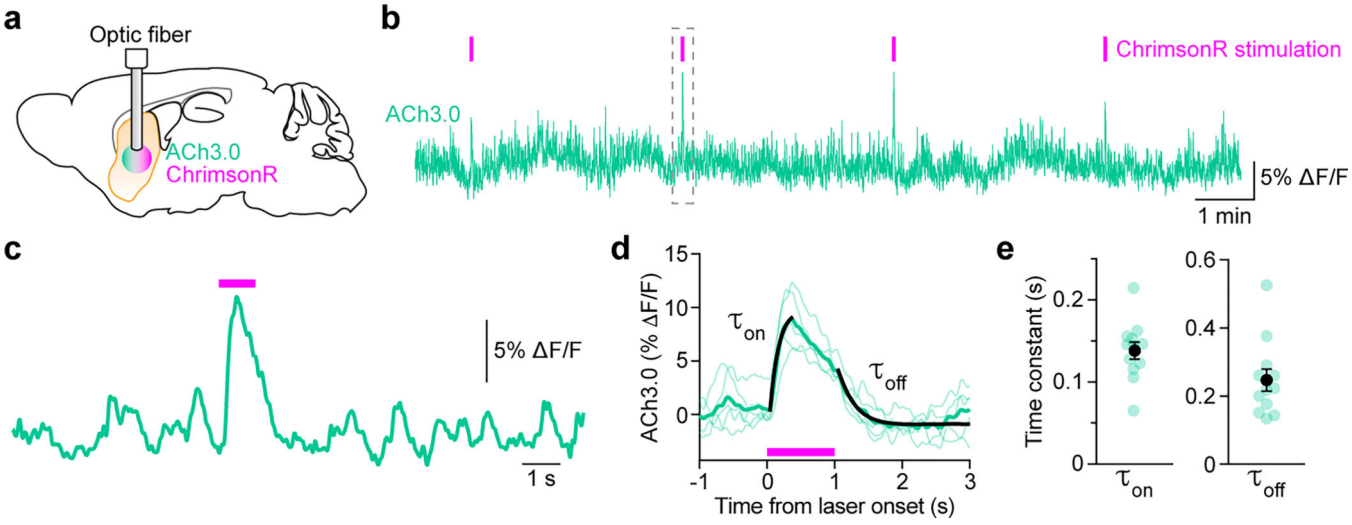

Extended Data Fig. 2. Kinetics of ACh3.0 sensor in the striatum *in vivo*.

a, Experimental preparation to optogenetically evoke ACh release *in vivo* using ChrimsonR while simultaneously monitoring ACh levels with ACh3.0 photometry via the same fiber optic. ChrimsonR and ACh3.0 were both virally-expressed. **b**, Example ACh3.0 recording (teal). ChrimsonR was stimulated every 200 s with 635 nm light flashes (20 Hz, 1 s; shown in magenta). **c**, detail of dashed box in **b** showing ChrimsonR-evoked ACh release. **d**, Overlay of individual ACh3.0 transients (light teal) from **b** aligned to optogenetic stimulation onset. Group mean shown in dark teal with overlaid exponential fits used to calculate onset (τ_{on}) and offset (τ_{off}) time constants in black. **e**, ACh3.0 τ_{on} (*left*) and τ_{off} (*right*). Mean (± s.e.m.) shown in black (τ_{on}: 138 ± 10 ms; τ_{off}: 247 ± 32 ms; n = 12 trials from 3 mice).

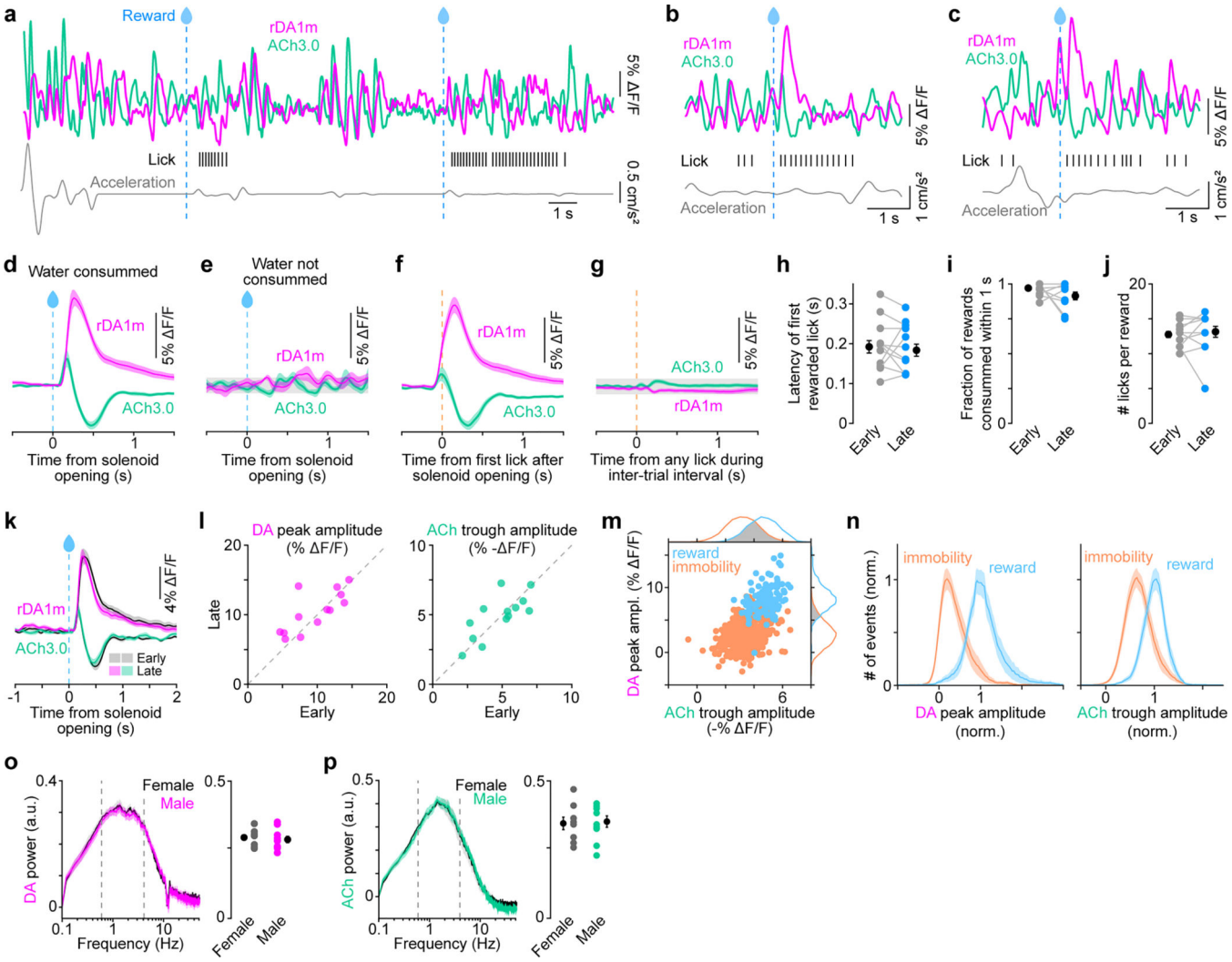

Extended Data Fig. 3. Reward-evoked DA and ACh responses in the DLS.

a, Example continuous recording of rDA1m (magenta) and ACh3.0 (teal) fluorescence, lick events (black) and treadmill acceleration (gray) illustrating the temporal dynamics of both sensors. Dashed blue lines depict uncued solenoid valve opening, which in this example did not generate large DA and ACh reward transients. **b**, Other reward response from same mouse. **c**, Example DA and ACh reward responses for a different mouse. **d**, Mean rDA1m (magenta) and ACh3.0 (teal) fluorescence aligned to solenoid valve opening for all uncued water deliveries followed within 1 s by consummatory licking (n = 13 mice). **e**, Same as **d** for water deliveries not followed by consummatory licking. Gray: 95% confidence interval. **f**, Same as **d**, but aligned to first lick after solenoid valve opening (i.e., first rewarded lick). **g**, Mean rDA1m and ACh3.0 fluorescence aligned to licks occurring between consummatory licking bouts (i.e., unrewarded licks). Gray: 95% confidence interval. **h-j**, Latency of first rewarded lick from solenoid valve opening (**h**; p = 0.52), fraction of rewards consumed within 1 s of valve opening (**i**; p = 0.14) and number of consummatory licks per reward delivery (**j**; p = 0.59) during the first (early) and last (late) quartiles of each imaging session in n = 13 mice suggest that the motivation to consume rewards is stable. **k**, Mean

reward-aligned DA and ACh responses imaged during the first (early; gray) and last (late; colored) quartiles of each imaging session are similar in amplitude and kinetics (n = 13 mice). **l**, Scatterplot of the mean amplitude of reward-evoked DA peaks (*left*; p=0.24) and ACh throughs (*right*; p = 0.74) at the beginning (early) vs. end (late) of each imaging session (n = 13 mice). **m**, Scatterplot of the amplitude of individual DA peaks and concurrent ACh troughs imaged during reward (blue) and periods of immobility (orange) in one example recording session. Amplitude distribution for ACh (*top*) and DA (*right*) with overlap shown in gray. **n**, Mean distribution of DA peak (*left*) and ACh trough (*right*) amplitudes for all mice (n = 13) normalized to the mode of reward distributions showing considerable overlap between reward and immobility states. **o**, *Left*, power spectrum of DA signal recorded in the DLS during immobility in n = 10 female mice (black) and n = 8 male mice (magenta). *Right*, Area under the curve of DA power spectra in the 0.5–4 Hz frequency band (p = 0.65). **p**, Same as **o**, for ACh (p = 0.84). Group means (± s.e.m.) in **h-j**, **o** and **p** are shown in black. Shaded regions in **d-g**, **k**, **n**, **o** and **p** denote s.e.m. Statistical comparisons are Student's paired *t*-tests in **h-j** and **l**, and Student's two-sample *t*-tests in **o** and **p**.

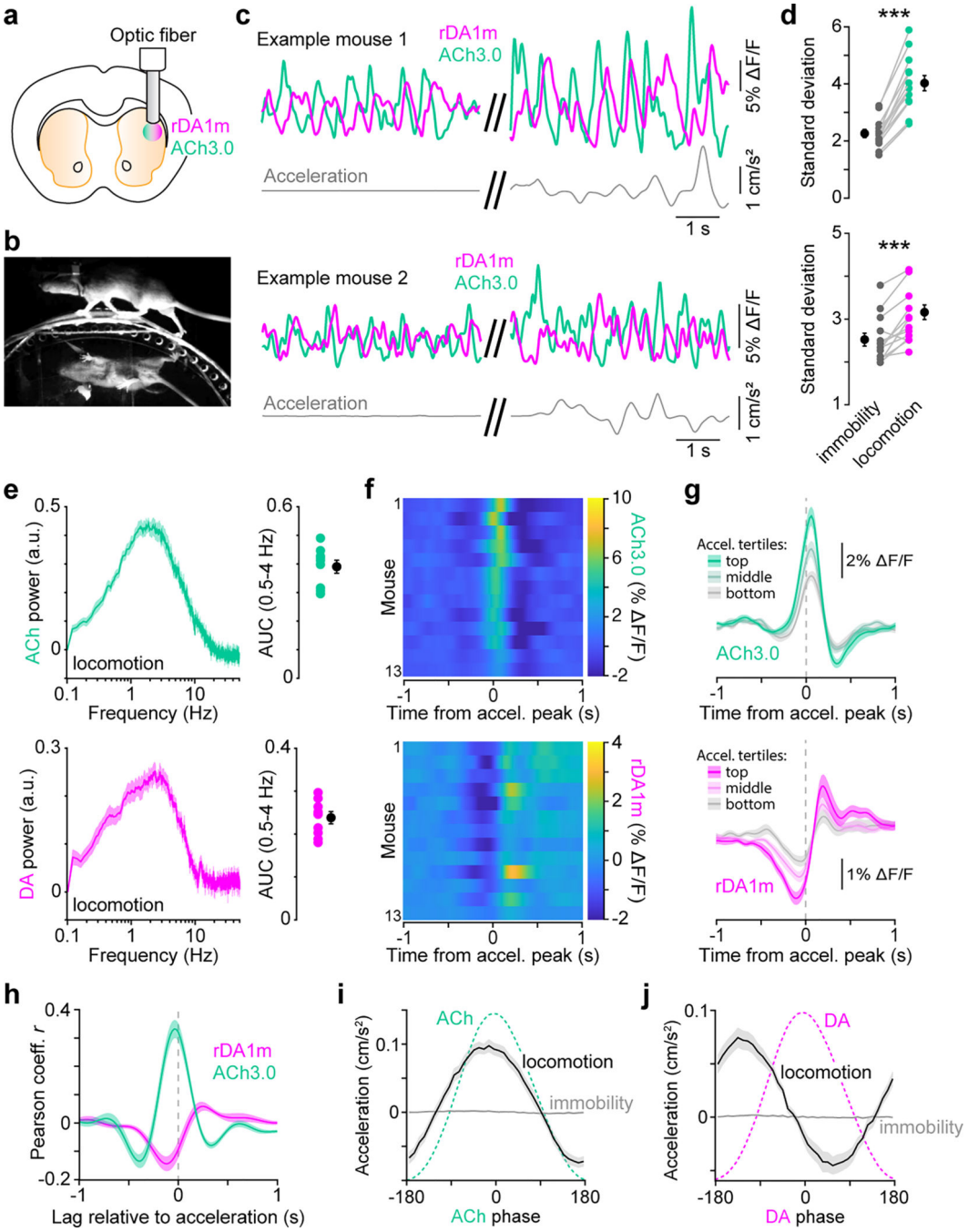

Extended Data Fig. 4. Locomotion-evoked DA and ACh responses in the DLS.

a-b, Experimental setup: virally-expressed rDA1m and ACh3.0 were imaged in the DLS (**a**) of mice head-fixed on a transparent cylindrical treadmill (**b**). **c**, Example rDA1m and ACh3.0 fluorescence from 2 separate mice during immobility (*left*) and spontaneous locomotion on the treadmill (*right*). **d**, Mean standard deviation of photometry signal during immobility and locomotion for ACh3.0 (*top*; $p=6.5\times10^{-8}$, Student's paired *t*-test) and rDA1m (*bottom*; $p=3.6\times10^{-4}$; Student's paired t-test). Group mean (± s.e.m.) shown in black (n = 13 mice). **e**, *Left*, mean ACh (*top*) and DA (*bottom*) power density

spectrum during locomotion (n = 13 mice). *Right*, Area under the curve (AUC) in 0.5–4 Hz frequency band. Group mean (± s.e.m.) shown in black. **f**, Heatmap of mean ACh3.0 (*top*) and rDA1m (*bottom*) fluorescence aligned to momentary peaks in treadmill acceleration during locomotion across mice. **g**, Group-averaged ACh3.0 (*top*) and rDA1m (*bottom*) fluorescence aligned to acceleration peaks stratified into tertiles according to acceleration magnitude. ACh and DA levels co-vary with acceleration magnitude. ACh levels peaking near acceleration maxima, whereas DA levels dip shortly before and crest shortly after acceleration maxima. **h**, Mean cross-correlation between treadmill acceleration and either ACh3.0 (teal) or rDA1m (magenta) fluorescence (n = 13 mice). **i**, Mean treadmill acceleration at different phases of periodic ACh fluctuations (dashed teal line) in the 0.5–4 Hz frequency band during locomotion (black) or immobility (gray) in n = 13 mice. During locomotion, periodic ACh fluctuations occur in phase with positive treadmill acceleration. Note that periodic ACh fluctuations during immobility are not associated with movements of the treadmill. **j**, Same as **i** for DA fluorescence. Note that DA fluctuations are phase-delayed relative to treadmill acceleration during locomotion, and not associated with micro-movements of the treadmill during immobility. Shaded regions in **e**, **g**-**j** denote s.e.m.

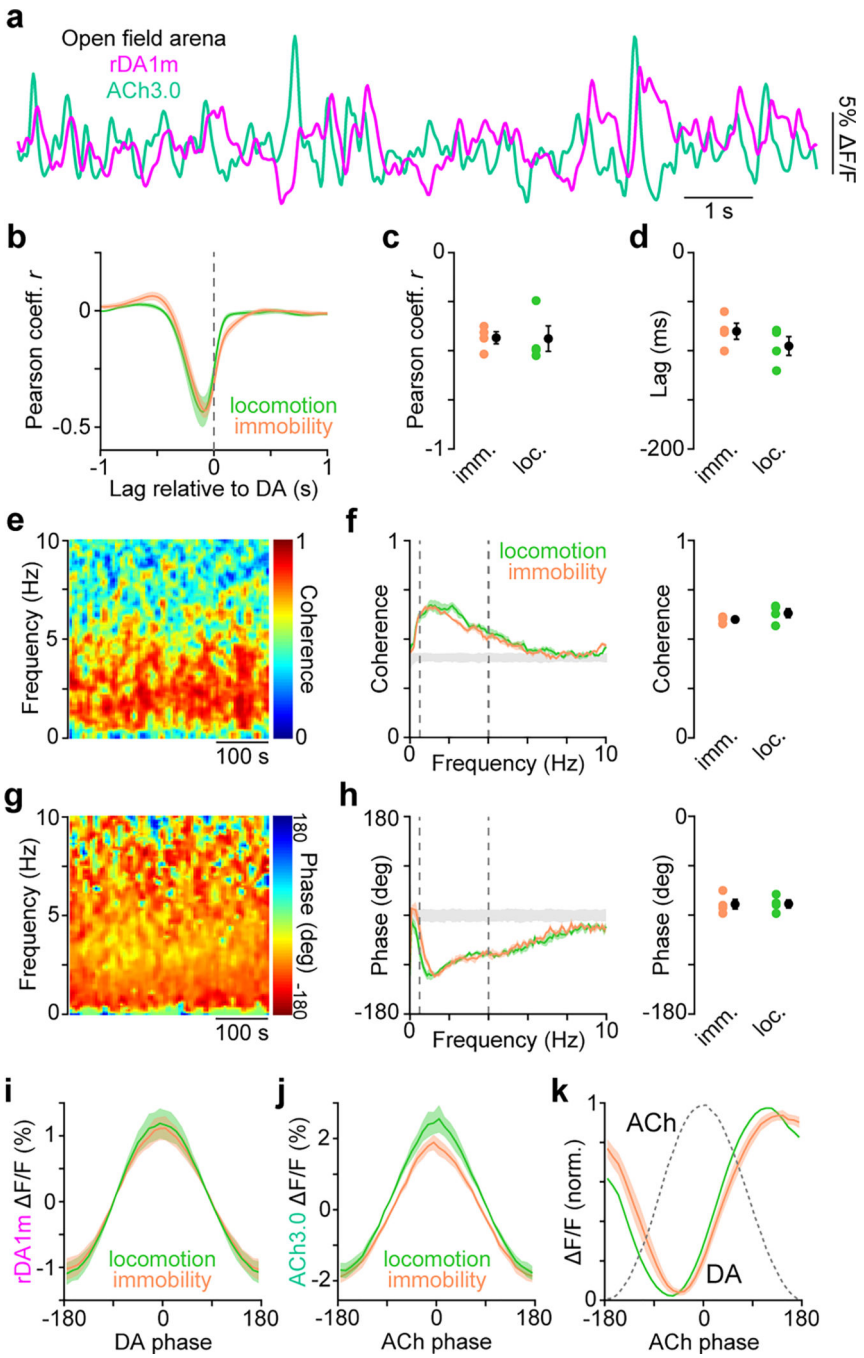

Extended Data Fig. 5. Spontaneous fluctuations in striatal DA and ACh in unrestrained mice.

a, Simultaneous photometry recording of rDA1m (magenta) and ACh3.0 (teal) fluorescence from a mouse in an open field arena. **b**, Mean cross-correlation between simultaneously recorded DA and ACh during locomotion (green) and immobility (orange) in n = 4 mice. **c**, Peak correlation coefficient between DA and ACh (p = 0.93) during immobility and locomotion (n = 4 mice). **d**, Same as **c** for time lag of negative cross-correlation peak (p = 0.06). **e**, Example coherence between DA and ACh signals across frequency and time domains during a recording in an open field arena. **f**, *Left*, mean coherence between DA and

ACh at different frequencies (n = 4 mice). Vertical lines depict 0.5 and 4 Hz. *Right*, median coherence in 0.5–4 Hz frequency band in individual mice (p = 0.25). **g-h**, Same as **e-f** for phase offset between DA and ACh (p = 0.93). **i**, Mean DA fluorescence at different phases of periodic DA fluctuations in the 0.5–4 Hz frequency band (n = 4 mice). **j**, Same as **h** for ACh fluorescence. **k**, Peak-normalized DA fluorescence vs. phase of periodic ACh fluctuations (gray dotted line) in 0.5–4 Hz frequency band during locomotion (green) and immobility (orange). Group means (± s.e.m.) in **c**, **d**, **f** and **h** shown in black. Shaded areas in **b**, **f**, **h-k** reflect s.e.m. All statistical comparisons are Student's paired *t*-tests.

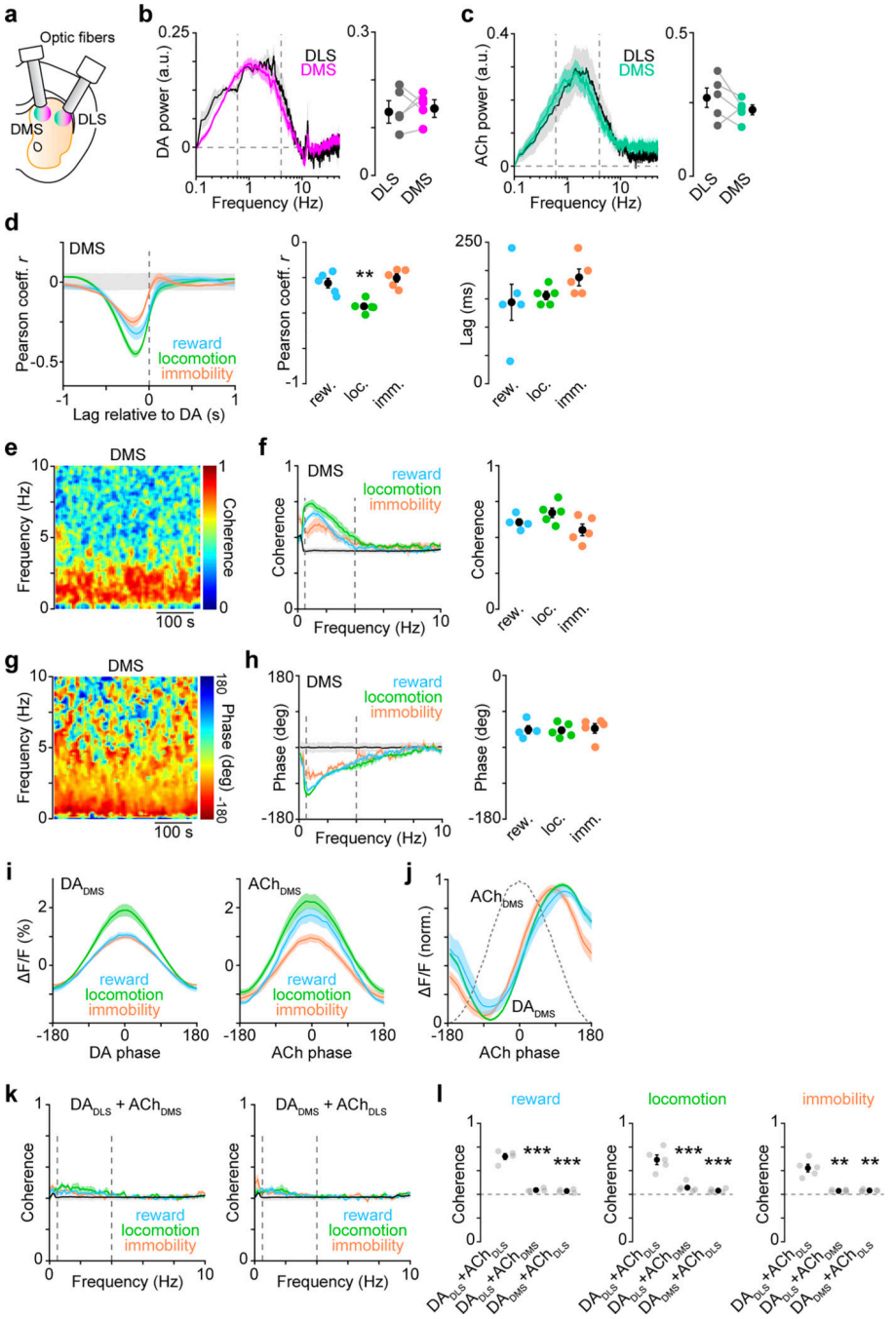

Extended Data Fig. 6. DA and ACh levels also fluctuate periodically in DMS.

a, Experimental setup. **b**, *Left*, mean power spectrum of DA signal recorded simultaneously from DMS (magenta) and DLS (black) during immobility in n = 5 mice. *Right*, area under the DA power spectra in the 0.5–4 Hz frequency band in DMS and DLS. Group averages (± s.e.m.) shown in black (p = 0.8, Student's paired *t*-test). **c**, Same as **b** for ACh (p = 0.3). **d**, *Left*, mean cross-correlation between DA and ACh in DMS across different behavioral states. *Middle*, peak correlation coefficient (Pearson's *r*) in individual mice. Group averages (± s.e.m.) shown in black (**p = 0.006 vs. reward and immobility,

one-way balanced ANOVA, Dunn's multiple comparisons; n = 5 mice). *Right*, time lag of negative cross-correlation peak (p = 0.4, one-way balanced ANOVA). **e**, Magnitude of coherence between DA and ACh in DMS across frequency and time domains for an example recording. **f**, *Left*, mean coherence at different frequencies across behavioral states (n = 5 mice). Vertical lines depict 0.5 and 4 Hz. *Right*, median coherence in 0.5–4 Hz frequency band in individual mice. Group averages (± s.e.m.) shown in black (p = 0.09, one-way unbalanced ANOVA; n = 5 mice). **g**, Same as **e** for phase offset between DA and ACh in DMS. **h**, Same as **f** for phase offset between DA and ACh in DMS (p = 0.2, one-way unbalanced ANOVA). **i**, *Left*, mean DA fluorescence at different phase of DA fluctuations in the 0.5–4 Hz frequency band in DMS. *Right*, same for ACh fluorescence vs. phase of ACh fluctuations. **j**, Peak-normalized DA fluorescence vs. phase of ACh in DMS. **k**, *Left*, mean coherence between simultaneously recorded DA_{DLS} and ACh_{DMS} (n = 5 mice). *Right*, same for coherence between DA_{DMS} and ACh_{DLS}. **l**, Median coherence in 0.5–4 Hz band in individual mice. Group averages (± s.e.m.) shown in black (reward: DA_{DLS}+ACh_{DMS} $p = 8.14\times10^{-7}$; DA_{DMS}+ACh_{DLS} $p = 6.07\times10^{-7}$; locomotion: DA_{DLS}+ACh_{DMS} $p = 7.46\times10^{-5}$; DA_{DMS}+ACh_{DLS} $p = 6.07\times10^{-5}$; immobility: DA_{DLS}+ACh_{DMS} p = 0.004; DA_{DMS}+ACh_{DLS} p = 0.005; all vs. DA_{DLS}+ACh_{DLS}, one-way unbalanced ANOVA, Dunn's multiple comparisons; n = 5 mice). Shaded areas in **b-d**, **f**, **h-k** reflect s.e.m.

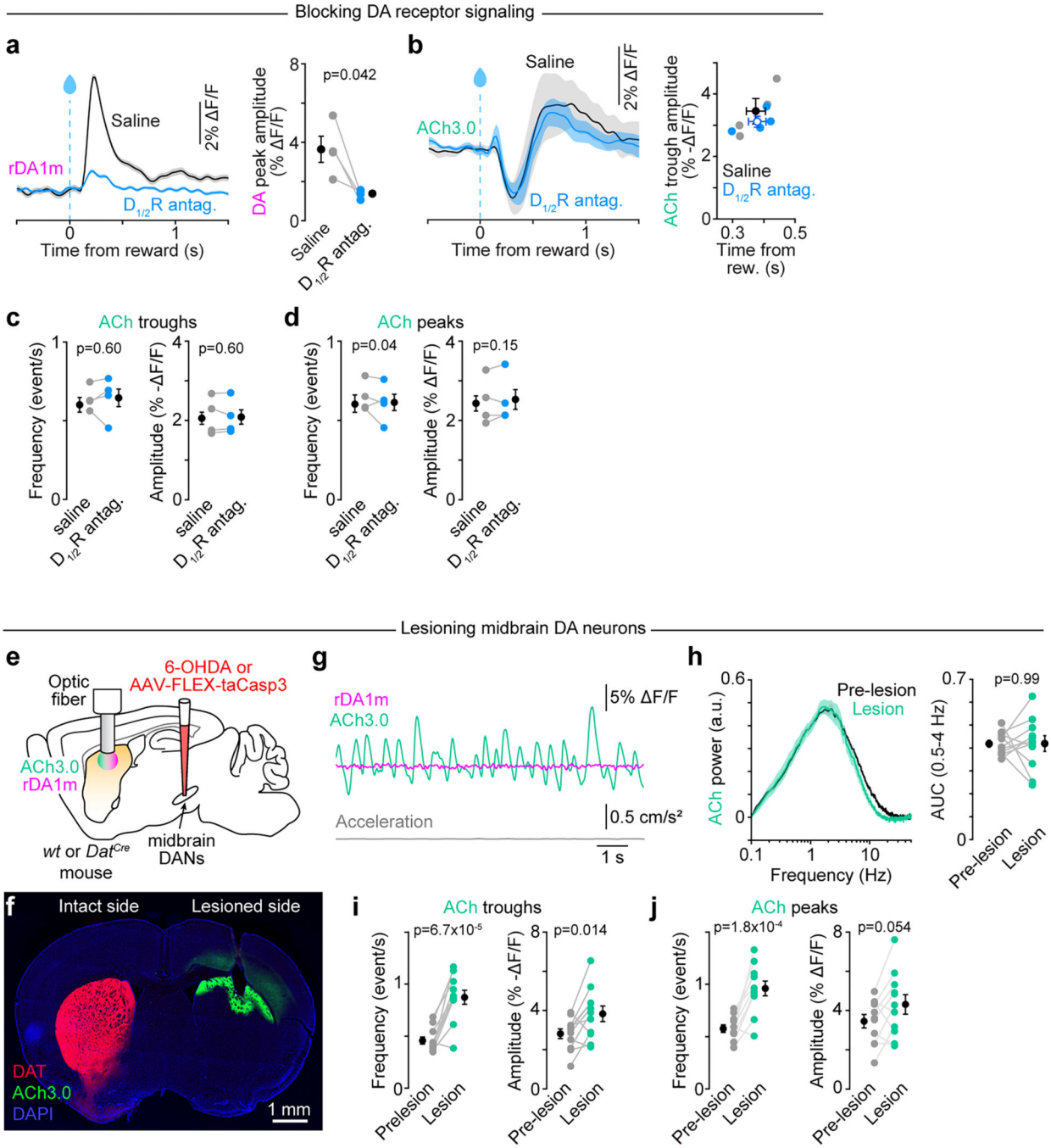

Extended Data Fig. 7. DA does not drive spontaneous fluctuations in ACh.

a, *Left*, example session-averaged DA fluorescence aligned to solenoid valve opening for all uncued water deliveries followed within 1 s by consummatory licking after intra-striatal infusion of saline (black) or a cocktail of D1 and D2 receptor antagonists (blue). *Right*, mean reward-evoked DA amplitude (n = 4 mice). **b**, *Left*, same as **a** for ACh. *Right*, scatter plot of mean reward-evoked ACh dip amplitude and timing in mice infused with saline or D1/2R antagonists (amplitude: p = 0.2; timing: p = 0.9, both vs. saline). **c**, Frequency (*left*) and amplitude (*right*) of spontaneous dips in ACh fluorescence during

immobility (n = 4 mice). **d**, Same as c for peaks in ACh. **e**, Experimental preparation to lesion midbrain DA neurons (DANs) unilaterally while imaging DA and ACh in the DLS ipsilaterally. DANs were lesioned using either 6OHDA infusions in wild type mice (n = 7), or AAV-mediated expression of Cre-dependent caspase-3 (AAV-FLEX-taCasp3) in the midbrain DANs of Dat^{Cre} mice (n = 4). **f**, Epifluorescence image of ACh3.0 (green) and DA transporter (DAT; red) immunofluorescence overlaid with DAPI nuclear stain (blue) in a coronal section from a Dat^{Cre} mouse injected with AAV-FLEX-taCasp3 into the right midbrain. Similar results were obtained in other 10 mice. **g**, Example DA (magenta) and ACh (teal) fluorescence following DAN lesion during immobility. **h**, *Left*, mean ACh power spectrum during immobility before (black) and after DAN lesion (teal; n = 11 mice). *Right*, ACh power area under the curve (AUC) in 0.5–4 Hz frequency band. **i**, Same as **c** before and after DAN lesion (n = 11 mice). Chronic DA depletion causes phasic dips in ACh to become larger and more frequent, hinting at a negative influence of DA on ACh release. **j**, Same as **d** before and after DAN lesion (n = 11 mice). Group means (± s.e.m.) in **a**-**d**, **h**-**j** are shown in black. Shaded areas in **a**, **b** and **h** reflect s.e.m. All statistical comparisons are Student's paired *t*-tests.

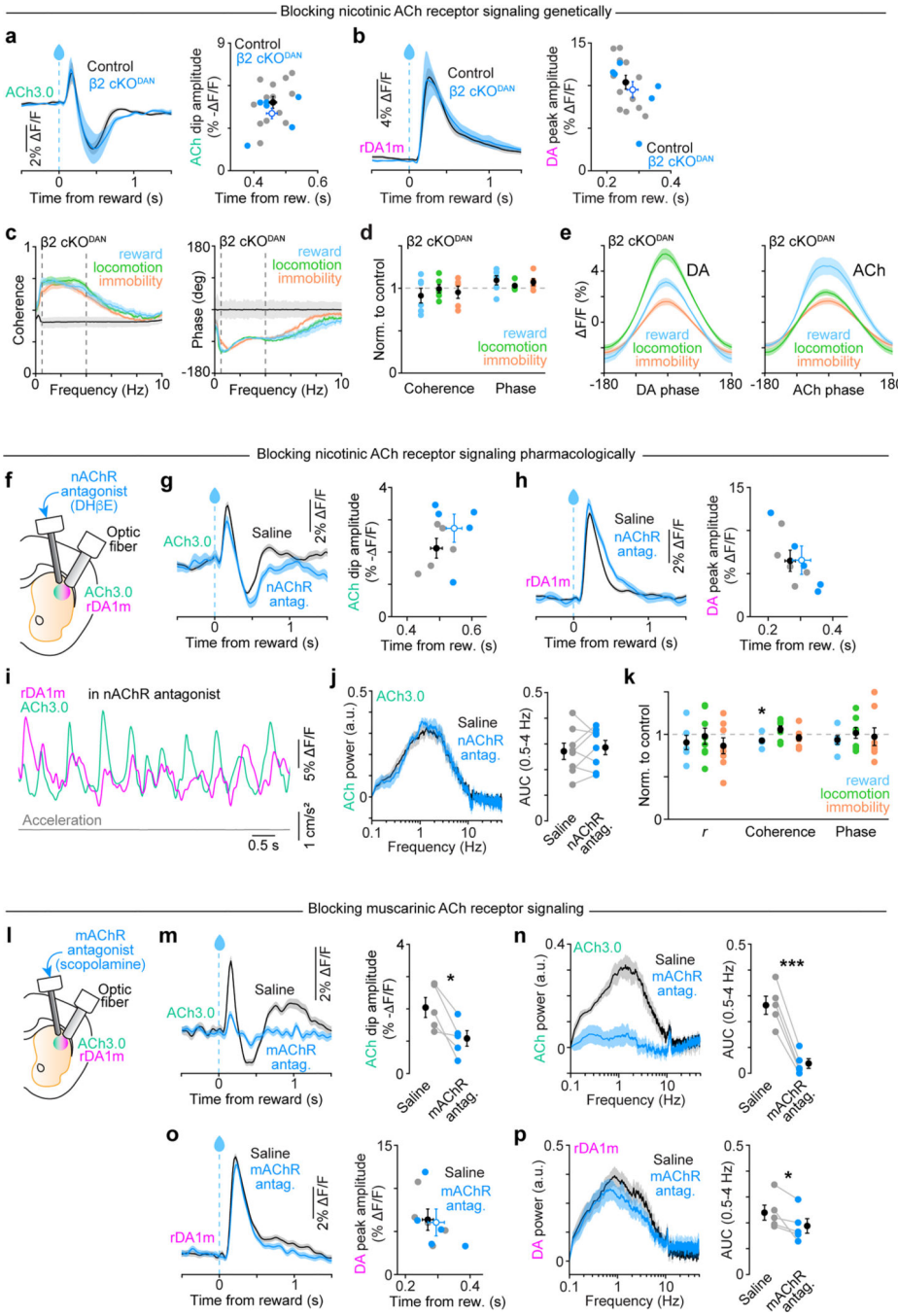

Extended Data Fig. 8. ACh signaling is not required for periodic DA fluctuations.

a, *Left*, example session-averaged ACh fluorescence aligned to solenoid opening for all uncued water deliveries followed within 1 s by consummatory licking in control (black) and β2 cKO^{DAN} (blue) mice. *Right*, scatter plot of mean reward-evoked ACh dip amplitude and timing in control (gray; n = 13) and β2 cKO^{DAN} (blue; n = 6) mice. Group means (± s.e.m.) overlaid (amplitude: p = 0.29; timing: p = 0.89, both vs. control, Student's two-sample *t*-test). **b**, *Left*, same as **a** for reward-evoked DA peak (amplitude: p = 0.58; timing, p = 0.33). **c**, *Left*, average coherence between DA and ACh signals in β2 cKO^{DAN} mice (n = 6)

at different frequencies during reward (blue), locomotion (green) and immobility (orange). Vertical lines depict 0.5 and 4 Hz. *Right*, same for phase offset. **d**, Median DA–ACh coherence and phase in 0.5–4 Hz band in β2 cKO^{DAN} mice (n = 6) normalized to control mice across conditions (coherence: reward p = 0.9, locomotion p = 0.3, immobility p = 0.9; phase: reward p = 0.4, locomotion p = 0.6, immobility p = 0.2; all comparisons vs. control, Student's two-sample *t*-test). Group mean (± s.e.m.) shown in black. **e**, *Left*, average DA fluorescence at different phases of periodic DA fluctuations in the 0.5–4 Hz frequency band across behavioral states in β2 cKO^{DAN} mice (n = 6 mice). *Right*, same for ACh fluorescence vs. phase of periodic ACh fluctuations. **f**, Experimental preparation for local pharmacological inhibition of nAChR signaling. **g**, Same as **a** after DLS infusion of saline (black) or the nAChR antagonist DHβE (blue; amplitude: p = 0.4; timing: p = 0.13, both vs. saline, Student's paired *t*-test, n = 5 mice). **h**, Same as **g** for DA (amplitude: p = 0.9; timing: p = 0.15). **i**, Example DA (magenta) and ACh (teal) traces during infusion of DHβE. **j**, *Left*, mean ACh power spectrum during immobility following intra-striatal infusion of saline (black) or DHβE (blue; n = 8 mice). *Right*, ACh power area under the curve **(**AUC**)** in 0.5–4 Hz frequency band (p = 0.6, Student's paired *t*-test). **k**, Same as **d** for Pearson's correlation coefficient *r* (reward: p = 0.2, locomotion: p = 0.5, immobility: p = 0.06), coherence (reward: p = 0.04, locomotion: p = 0.6, immobility: p = 0.09) and phase (reward: p = 0.2, locomotion: p = 0.5, immobility: p = 0.6) in DHβE normalized to saline (all comparisons vs. saline, Student's paired *t*-test; n = 8 mice). **l**, Experimental preparation for local pharmacological inhibition of mAChR signaling in the DLS. **m**, *Left*, same as **g** following infusion of saline (black) or the mAChR antagonist scopolamine (blue). *Right*, amplitude of reward-evoked dip in ACh fluorescence (p = 0.02; n = 5 mice). **n**, same as **j** after infusion of saline or mAChR antagonist (p = 2.5×10^{-4}, Student's paired *t*-test; n = 5 mice). This effect confirms that scopolamine reaches the volume of tissue imaged by the fiber optic. **o**, Same as **m** for DA (amplitude: p = 0.6, timing: p = 0.09; n = 5 mice). **p**, Same as **n** for DA (p = 0.048). This effect is consistent with the role of facilitatory effects of presynaptic mAChRs on DAN axons (see ref. [31]). Shaded areas in **a**, **b**, **c**, **e**, **g**, **h**, **j** and **m-p** reflect s.e.m.

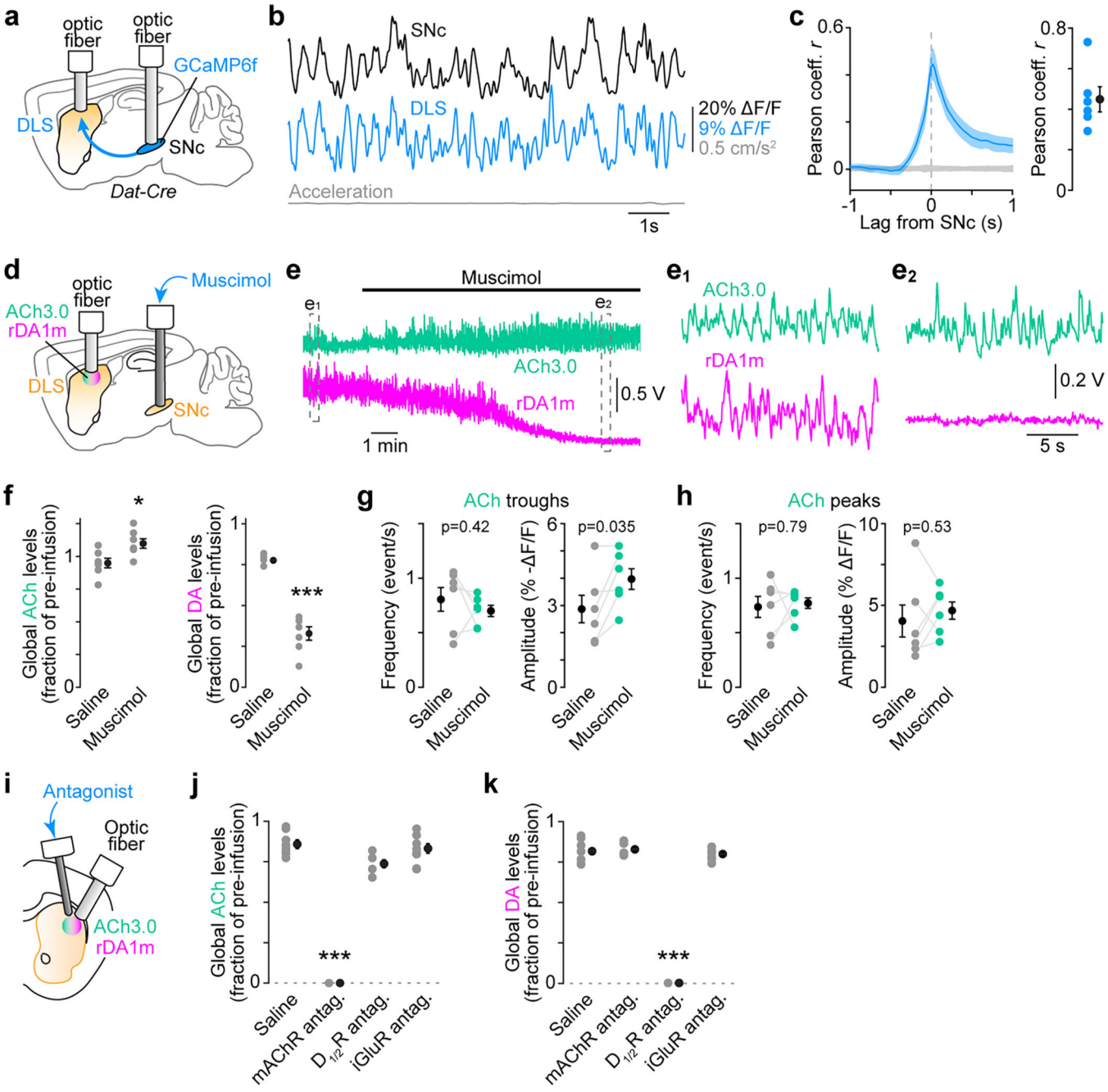

Extended Data Fig. 9. Midbrain DAN activity underlies periodic fluctuations in striatal DA.

a, Experimental preparation for simultaneously imaging the activity of DANs in the SNc and their axons in the DLS. **b**, Example photometry recording of GCaMP6f in the SNc (black) and DLS (blue) during immobility. **c**, *Left*, average (± s.e.m. shown as shaded region) cross-correlation between SNc and DLS signals during immobility in n = 6 mice. 95% confidence interval shown in gray. *Right*, peak correlation coefficient between SNc and DLS signals. Group mean (± s.e.m.) in black. **d**, Experimental preparation for pharmacological silencing of SNc while imaging of rDA1m and ACh3.0 in the DLS. **e**, *Left*, Example continuous recording of ACh3.0 (teal) and rDA1m (magenta). Black line

depicts muscimol infusion. *Right*, Detail of dashed boxes showing ACh and DA fluctuations during immobility before (**e**$_1$) and following (**e**$_2$) infusion of muscimol. Note that muscimol abolishes phasic DA transients as well as 'global' DA levels in the DLS, whereas ACh global levels and phasic transients persist. **f**, Average global ACh and DA fluorescence during immobility after infusion of saline and muscimol. Group mean (± s.e.m.) shown in black (ACh: p = 0.021; DA: p = 0.0001, Student's paired *t*-test; n = 6 mice). **g**, Frequency (*left*) and amplitude (*right*) of spontaneous dips in ACh fluorescence recorded during immobility after infusion of saline (gray) or muscimol (teal). Group mean (± s.e.m.) shown in black (n = 6 mice). p-values (Student's paired *t*-tests) indicated in figure. **h**, Same as **g** for peaks in ACh fluorescence. Collectively, these data confirm that spontaneous DA fluctuations in the DLS are driven by the somatic activity of midbrain DANs, whereas spontaneous ACh transients do not require DAN activity. **i**, Experimental preparation for local pharmacological inhibition of neurotransmitter receptors in the DLS. **j**, Average global ACh fluorescence measured during immobility after intra-striatal infusion of saline, the mAChR antagonist scopolamine ($p = 6.9\times10^{-6}$; n = 5 mice), the D1/2R antagonists SCH23390 and sulpiride (p = 0.24; n = 4 mice) or the iGluR antagonists NBQX and APV (p = 0.41; n = 8 mice; all comparisons are Student's paired *t*-test vs. saline control). Data are expressed as a fraction of global ACh fluorescence pre-infusion. Group means (± s.e.m.) are shown in black. Note that mAChR antagonist blocks ACh3.0 (and therefore serves a positive control for maximal possible change in ACh signal) and that blocking iGluRs in the DLS does not significantly alter overall ACh3.0 fluorescence compared to saline, suggesting that CINs continue to release ACh via spontaneous, cell-autonomous firing. **k**, Same as **l** for global DA fluorescence after infusion of saline, scopolamine (p = 0.24), D1/2R antagonists ($p = 1.1\times10^{-4}$) or iGluR antagonists (p = 0.53). Note that blocking iGluRs in the DLS does not alter overall rDA1m fluorescence either, suggesting that DA axons continue to release DA.

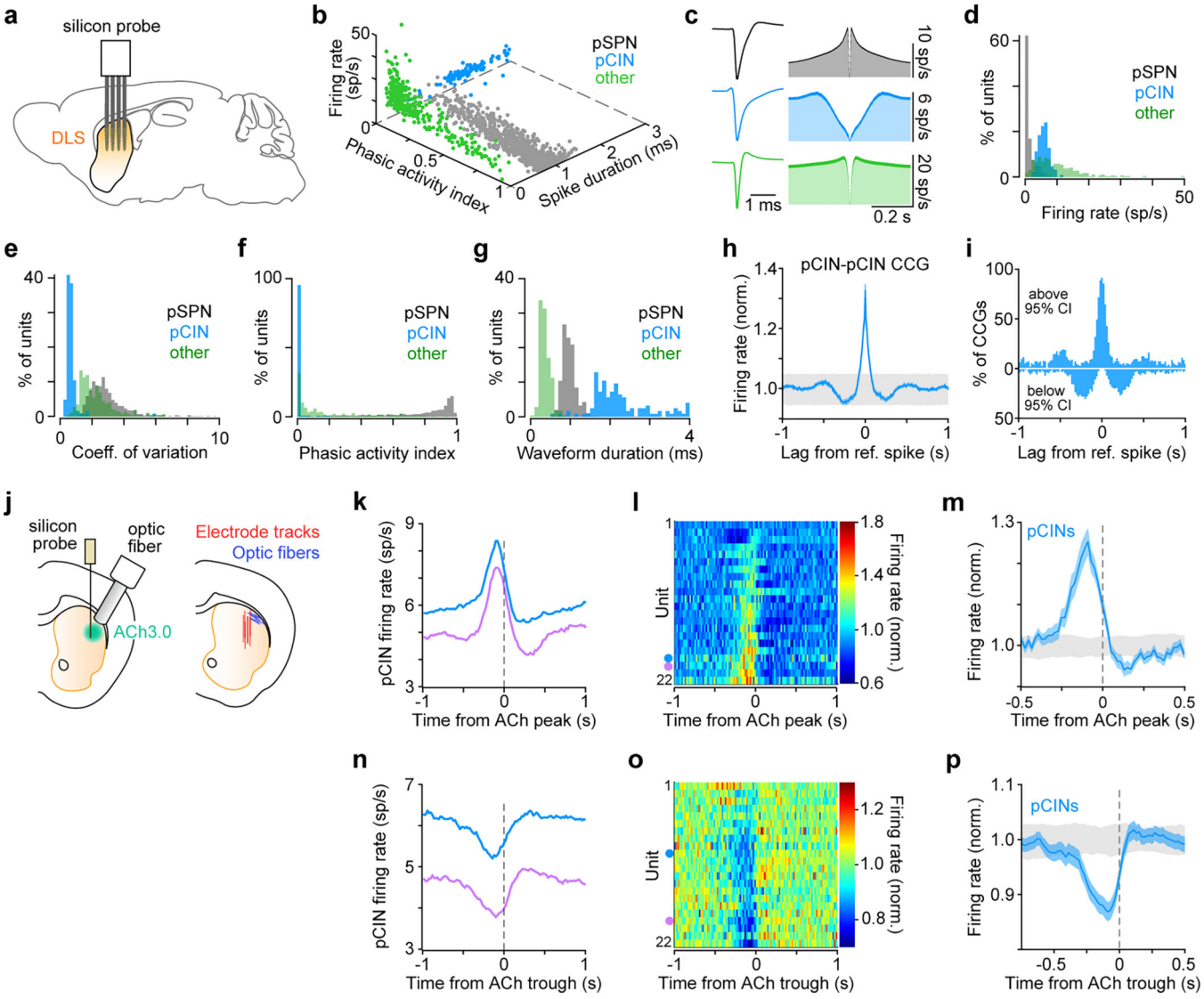

Extended Data Fig. 10. Characterization of electrophysiological recordings in the DLS.

a, Experimental preparation for acute *in vivo* extracellular recordings in the DLS. **b**, Scatter plot of spike properties used to distinguish units as putative SPNs (pSPNs; gray), putative CINs (pCINs; blue), or other putative interneurons (green). **c**, Average waveform (left) and auto-correlograms (right) for pSPNs (black), pCINs (blue), and other neurons (green). **d-g**, Distribution of firing rates (**d**), coefficient of variation of inter-spike intervals (**e**), phasic activity index (**f**), and waveform duration for pSPNs (black), pCINs (blue), and other neurons (green). **h**, Mean (± s.e.m.) pCIN-pCIN cross correlogram (CCG) computed from all units shown in Fig. 4c (n = 157 pairs). 95% confidence interval shown in gray. **i**, Proportion of CCGs from Fig. 4c with firing rates above or below the 95% confidence interval (bin size: 20 ms). **j**, *Left*, experimental preparation for simultaneous ACh photometry and acute *in vivo* extracellular recordings from the DLS. *Right*, location of all recovered fiber optic implant tips (blue) and electrode tracks (red) in the DLS merged across anterior-posterior levels +0.5 to 0.75 mm relative to bregma. **k**, Men firing rate of two

simultaneously recorded pCIN units aligned to ACh fluorescence peaks during immobility. **l**, Instantaneous (mean normalized) firing rate of pCINs (n = 22) aligned to ACh fluorescence peaks during immobility. Dots indicate units shown in **k**. **m**, Average firing rate (normalized to mean; ± s.e.m. shown in shaded region) of all pCINs shown in **l**. 95% confidence interval shown in gray. **n-p**, Same as **k-m** aligned to ACh fluorescence troughs.

Acknowledgments

We thank G. Buzsaki, M. Long, S. Shoham, R. Tsien and members of the Tritsch laboratory for comments on the manuscript, M. Crair (Yale) and R. Machold (NYULH) for providing the $\beta 2^{\text{floxed}}$ and $ChAT^{\text{floxed}}$.$Nkx2.1^{\text{Cre}}$ mice, respectively. This work was supported by the National Institutes of Health (DP2NS105553 and R01MH130658 to N.X.T; T32NS086750, T32GM007308 and T32GM136573 to A.C.K), the Paolo and Marlene Fresco, Alfred P. Sloan, Dana, Whitehall and Feldstein Medical Foundations to N.X.T and a Vilcek Scholars Award to A.C.K. We acknowledge the New York University Langone Health Rodent Genetic Engineering Laboratory for rederivation, the Genotyping Core Laboratory for mouse genotyping, the Department of Comparative Medicine for animal care and maintenance and the Neuroscience Institute's imaging facilities for microscope availability. We apologize to those whose work we were unable to cite due to length limits.

Data availability

The data that support the findings of this study are available from the corresponding author upon reasonable request.

References

1. Schultz W. Behavioral theories and the neurophysiology of reward. Annu Rev Psychol 57, 87–115 (2006). [PubMed: 16318590]
2. O'Doherty JP, Cockburn J. & Pauli WM Learning, Reward, and Decision Making. Annu Rev Psychol 68, 73–100 (2017). [PubMed: 27687119]
3. Mirenowicz J. & Schultz W. Preferential activation of midbrain dopamine neurons by appetitive rather than aversive stimuli. Nature 379, 449–451 (1996). [PubMed: 8559249]
4. Cohen JY, Haesler S, Vong L, Lowell BB & Uchida N. Neuron-type-specific signals for reward and punishment in the ventral tegmental area. Nature 482, 85–88 (2012). [PubMed: 22258508]
5. Morris G, Arkadir D, Nevet A, Vaadia E. & Bergman H. Coincident but distinct messages of midbrain dopamine and striatal tonically active neurons. Neuron 43, 133–143 (2004). [PubMed: 15233923]
6. Aosaki T, Graybiel AM & Kimura M. Effect of the nigrostriatal dopamine system on acquired neural responses in the striatum of behaving monkeys. Science 265, 412–415 (1994). [PubMed: 8023166]
7. Costa RM A selectionist account of de novo action learning. Curr Opin Neurobiol 21, 579–586 (2011). [PubMed: 21641793]
8. Coddington LT & Dudman JT Learning from Action: Reconsidering Movement Signaling in Midbrain Dopamine Neuron Activity. Neuron 104, 63–77 (2019). [PubMed: 31600516]
9. Berke JD What does dopamine mean? Nat Neurosci 21, 787–793 (2018). [PubMed: 29760524]
10. Klaus A, Alves da Silva J. & Costa RM What, If, and When to Move: Basal Ganglia Circuits and Self-Paced Action Initiation. Annu Rev Neurosci 42, 459–483 (2019). [PubMed: 31018098]
11. Cox J. & Witten IB Striatal circuits for reward learning and decision-making. Nat Rev Neurosci 20, 482–494 (2019). [PubMed: 31171839]
12. Shen W. et al. M4 Muscarinic Receptor Signaling Ameliorates Striatal Plasticity Deficits in Models of L-DOPA-Induced Dyskinesia. Neuron 88, 762–773 (2015). [PubMed: 26590347]
13. Reynolds JNJ et al. Coincidence of cholinergic pauses, dopaminergic activation and depolarisation of spiny projection neurons drives synaptic plasticity in the striatum. Nat Commun 13, 1296 (2022). [PubMed: 35277506]

14. Howe MW & Dombeck DA Rapid signalling in distinct dopaminergic axons during locomotion and reward. Nature 535, 505–510 (2016). [PubMed: 27398617]
15. da Silva JA, Tecuapetla F, Paixao V. & Costa RM Dopamine neuron activity before action initiation gates and invigorates future movements. Nature 554, 244–248 (2018). [PubMed: 29420469]
16. Panigrahi B. et al. Dopamine Is Required for the Neural Representation and Control of Movement Vigor. Cell 162, 1418–1430 (2015). [PubMed: 26359992]
17. Engelhard B. et al. Specialized coding of sensory, motor and cognitive variables in VTA dopamine neurons. Nature 570, 509–513 (2019). [PubMed: 31142844]
18. Mohebi A. et al. Dissociable dopamine dynamics for learning and motivation. Nature 570, 65–70 (2019). [PubMed: 31118513]
19. Howe M. et al. Coordination of rapid cholinergic and dopaminergic signaling in striatum during spontaneous movement. Elife 8 (2019).
20. Sulzer D, Cragg SJ & Rice ME Striatal dopamine neurotransmission: regulation of release and uptake. Basal Ganglia 6, 123–148 (2016). [PubMed: 27141430]
21. Threlfell S. et al. Striatal dopamine release is triggered by synchronized activity in cholinergic interneurons. Neuron 75, 58–64 (2012). [PubMed: 22794260]
22. Cachope R. et al. Selective activation of cholinergic interneurons enhances accumbal phasic dopamine release: setting the tone for reward processing. Cell Rep 2, 33–41 (2012). [PubMed: 22840394]
23. Liu C. et al. An action potential initiation mechanism in distal axons for the control of dopamine release. Science 375, 1378–1385 (2022). [PubMed: 35324301]
24. Straub C, Tritsch NX, Hagan NA, Gu C. & Sabatini BL Multiphasic modulation of cholinergic interneurons by nigrostriatal afferents. J Neurosci 34, 8557–8569 (2014). [PubMed: 24948810]
25. Chuhma N, Mingote S, Moore H. & Rayport S. Dopamine neurons control striatal cholinergic neurons via regionally heterogeneous dopamine and glutamate signaling. Neuron 81, 901–912 (2014). [PubMed: 24559678]
26. Sun F. et al. Next-generation GRAB sensors for monitoring dopaminergic activity in vivo. Nat Methods 17, 1156–1166 (2020). [PubMed: 33087905]
27. Jing M. et al. An optimized acetylcholine sensor for monitoring in vivo cholinergic activity. Nat Methods 17, 1139–1146 (2020). [PubMed: 32989318]
28. Tritsch NX & Sabatini BL Dopaminergic modulation of synaptic transmission in cortex and striatum. Neuron 76, 33–50 (2012). [PubMed: 23040805]
29. Hnasko TS et al. Vesicular glutamate transport promotes dopamine storage and glutamate corelease in vivo. Neuron 65, 643–656 (2010). [PubMed: 20223200]
30. Tritsch NX, Ding JB & Sabatini BL Dopaminergic neurons inhibit striatal output through non-canonical release of GABA. Nature 490, 262–266 (2012). [PubMed: 23034651]
31. Shin JH, Adrover MF, Wess J. & Alvarez VA Muscarinic regulation of dopamine and glutamate transmission in the nucleus accumbens. Proc Natl Acad Sci U S A 112, 8124–8129 (2015). [PubMed: 26080439]
32. Joshua M. et al. Synchronization of midbrain dopaminergic neurons is enhanced by rewarding events. Neuron 62, 695–704 (2009). [PubMed: 19524528]
33. Liu C, Goel P. & Kaeser PS Spatial and temporal scales of dopamine transmission. Nat Rev Neurosci 22, 345–358 (2021). [PubMed: 33837376]
34. Fujisawa S. & Buzsaki GA 4 Hz oscillation adaptively synchronizes prefrontal, VTA, and hippocampal activities. Neuron 72, 153–165 (2011). [PubMed: 21982376]
35. Watabe-Uchida M, Zhu L, Ogawa SK, Vamanrao A. & Uchida N. Whole-brain mapping of direct inputs to midbrain dopamine neurons. Neuron 74, 858–873 (2012). [PubMed: 22681690]
36. Guo Q. et al. Whole-brain mapping of inputs to projection neurons and cholinergic interneurons in the dorsal striatum. PLoS One 10, e0123381 (2015).
37. Neske GT Sleepy Circuits in Vigilant Mice? A Slow Cortical Oscillation Occurring during Multiple Arousal States. J Neurosci 37, 7294–7296 (2017). [PubMed: 28768793]

38. Nacher V, Ledberg A, Deco G. & Romo R. Coherent delta-band oscillations between cortical areas correlate with decision making. Proc Natl Acad Sci U S A 110, 15085–15090 (2013). [PubMed: 23980180]
39. Lee K. et al. Gain Modulation by Corticostriatal and Thalamostriatal Input Signals during Reward-Conditioned Behavior. Cell Rep 29, 2438–2449 e2434 (2019). [PubMed: 31747611]
40. Quick MW & Lester RA Desensitization of neuronal nicotinic receptors. J Neurobiol 53, 457–478 (2002). [PubMed: 12436413]
41. Maskos U. et al. Nicotine reinforcement and cognition restored by targeted expression of nicotinic receptors. Nature 436, 103–107 (2005). [PubMed: 16001069]
42. Choi SJ et al. Alterations in the intrinsic properties of striatal cholinergic interneurons after dopamine lesion and chronic L-DOPA. Elife 9 (2020).
43. Mamaligas AA, Barcomb K. & Ford CP Cholinergic Transmission at Muscarinic Synapses in the Striatum Is Driven Equally by Cortical and Thalamic Inputs. Cell Rep 28, 1003–1014 e1003 (2019). [PubMed: 31340139]
44. Zhang YF, Reynolds JNJ & Cragg SJ Pauses in Cholinergic Interneuron Activity Are Driven by Excitatory Input and Delayed Rectification, with Dopamine Modulation. Neuron 98, 918–925 e913 (2018). [PubMed: 29754751]
45. Beeler JA & Kisbye Dreyer J. Synchronicity: The Role of Midbrain Dopamine in Whole-Brain Coordination. eNeuro 6 (2019).
46. Shen W, Flajolet M, Greengard P. & Surmeier DJ Dichotomous dopaminergic control of striatal synaptic plasticity. Science 321, 848–851 (2008). [PubMed: 18687967]
47. Liu Y, Mattar MG, Behrens TEJ, Daw ND & Dolan RJ Experience replay is associated with efficient nonlocal learning. Science 372 (2021).
48. Graybiel AM The basal ganglia and chunking of action repertoires. Neurobiol Learn Mem 70, 119–136 (1998). [PubMed: 9753592]
49. Soares S, Atallah BV & Paton JJ Midbrain dopamine neurons control judgment of time. Science 354, 1273–1277 (2016). [PubMed: 27940870]
50. Liu Y, Nour MM, Schuck NW, Behrens TEJ & Dolan RJ Decoding cognition from spontaneous neural activity. Nat Rev Neurosci 23, 204–214 (2022). [PubMed: 35260845]
51. Patel JC, Rossignol E, Rice ME & Machold RP Opposing regulation of dopaminergic activity and exploratory motor behavior by forebrain and brainstem cholinergic circuits. Nat Commun 3, 1172 (2012). [PubMed: 23132022]
52. Burbridge TJ et al. Visual circuit development requires patterned activity mediated by retinal acetylcholine receptors. Neuron 84, 1049–1064 (2014). [PubMed: 25466916]
53. Backman CM et al. Characterization of a mouse strain expressing Cre recombinase from the 3' untranslated region of the dopamine transporter locus. Genesis 44, 383–390 (2006). [PubMed: 16865686]
54. Chen TW et al. Ultrasensitive fluorescent proteins for imaging neuronal activity. Nature 499, 295–300 (2013). [PubMed: 23868258]
55. Thiele SL, Warre R. & Nash JE Development of a unilaterally-lesioned 6-OHDA mouse model of Parkinson's disease. J Vis Exp (2012).
56. Yang CF et al. Sexually dimorphic neurons in the ventromedial hypothalamus govern mating in both sexes and aggression in males. Cell 153, 896–909 (2013). [PubMed: 23663785]
57. Warren RA et al. A rapid whisker-based decision underlying skilled locomotion in mice. Elife 10 (2021).
58. Yang L, Lee K, Villagracia J. & Masmanidis SC Open source silicon microprobes for high throughput neural recording. J Neural Eng 17, 016036 (2020).
59. Stanford Research Systems, About Lock-In Amplifiers (available at https://www.thinksrs.com/downloads/pdfs/applicationnotes/AboutLIAs.pdf).
60. Balakrishnan H. & Verghese G. Modulation and Demodulation (available at http://web.mit.edu/6.02/www/s2012/handouts/14.pdf).
61. Zutshi I, Valero M, Fernandez-Ruiz A. & Buzsaki G. Extrinsic control and intrinsic computation in the hippocampal CA1 circuit. Neuron 110, 658–673 e655 (2022). [PubMed: 34890566]

62. Berke JD, Okatan M, Skurski J. & Eichenbaum HB Oscillatory entrainment of striatal neurons in freely moving rats. Neuron 43, 883–896 (2004). [PubMed: 15363398]

63. Schmitzer-Torbert NC & Redish AD Task-dependent encoding of space and events by striatal neurons is dependent on neural subtype. Neuroscience 153, 349–360 (2008). [PubMed: 18406064]

64. Sharott A, Doig NM, Mallet N. & Magill PJ Relationships between the firing of identified striatal interneurons and spontaneous and driven cortical activities in vivo. J Neurosci 32, 13221–13236 (2012). [PubMed: 22993438]

65. Yamin HG, Stern EA & Cohen D. Parallel processing of environmental recognition and locomotion in the mouse striatum. J Neurosci 33, 473–484 (2013). [PubMed: 23303928]

66. Peters AJ, Fabre JMJ, Steinmetz NA, Harris KD & Carandini M. Striatal activity topographically reflects cortical activity. Nature 591, 420–425 (2021). [PubMed: 33473213]

67. Gage GJ, Stoetzner CR, Wiltschko AB & Berke JD Selective activation of striatal fast-spiking interneurons during choice execution. Neuron 67, 466–479 (2010). [PubMed: 20696383]

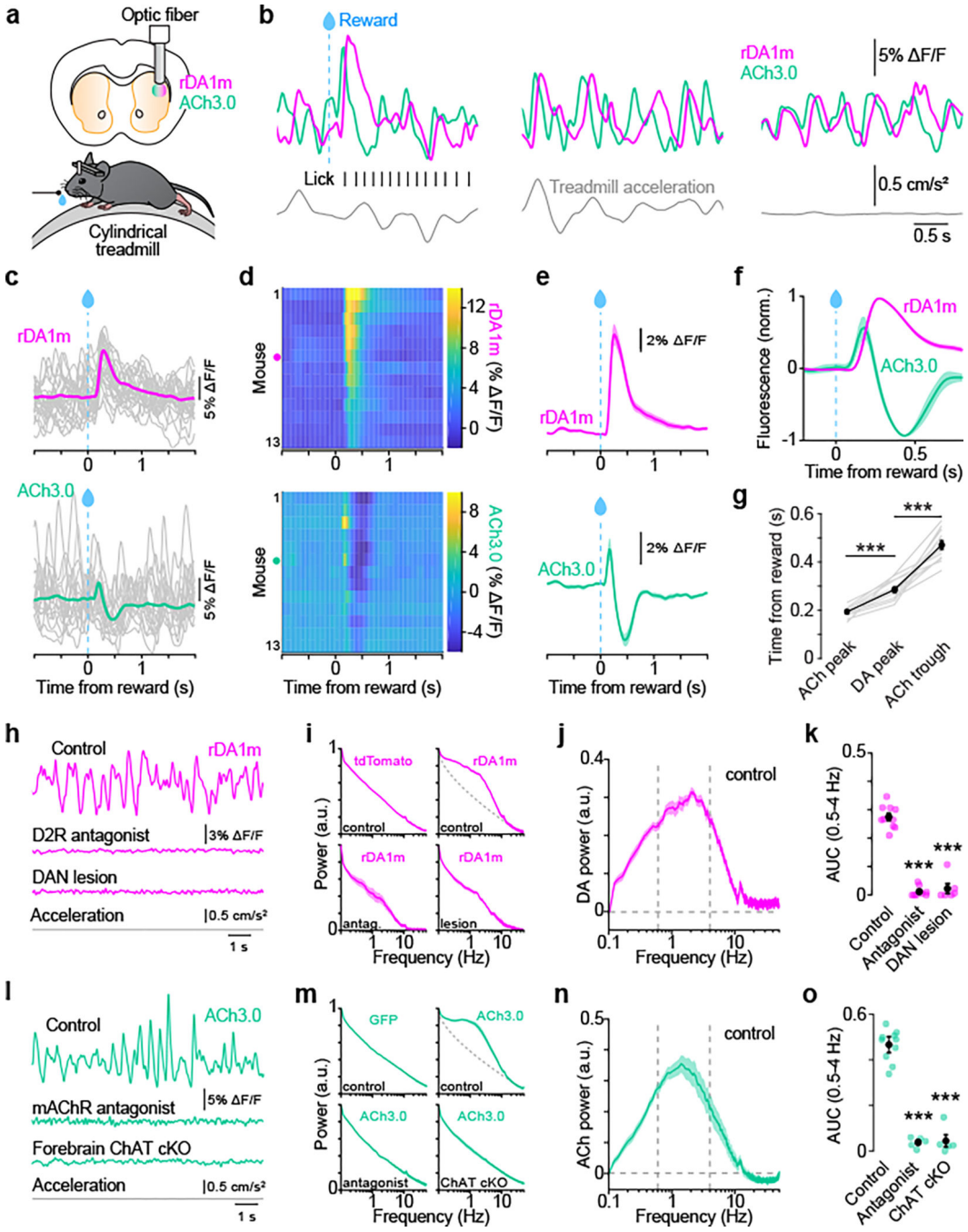

Fig. 1. Spontaneous periodic fluctuations in striatal DA and ACh.

a, Experimental setup to monitor DA and ACh levels in the DLS. **b**, Example rDA1m (magenta) and ACh3.0 (teal) fluorescence recorded during reward (*left*), locomotion (*middle*) and immobility (*right*). Black: licks, gray: treadmill acceleration. **c-e**, Session-averaged rDA1m (*top*) and ACh3.0 (*bottom*) signals aligned to solenoid valve opening (blue) in example mouse (**c**; gray: 20 randomly-selected single trials), in all recorded mice (**d**; dot: animal in **c**), and averaged across all 13 mice (**e**). **f**, Same as **e** normalized to rDA1m maxima and ACh3.0 minima. **g**, Latency of reward-evoked DA and ACh transients (ACh

peak vs. DA peak: $p = 2.5\times10^{-7}$; DA peak vs. ACh trough: $p = 9.6\times10^{-10}$; one-way balanced ANOVA, Dunn's multiple comparisons; n = 13 mice). Gray: individual mice. **h**, Example rDA1m fluorescence during immobility (*top*) following systemic treatment with the D2R antagonist sulpiride (*middle*) or midbrain DAN lesion with 6OHDA (*bottom*). Acceleration (gray) shown for control recording. **i**, Normalized power spectra of photometry signal for tdTomato (n = 3 mice) and rDA1m in control (n = 13), sulpiride-treated (n = 8) and 6OHDA-lesioned (n = 6) mice during immobility. **j**, Isolated power spectrum of DA signal. Vertical lines indicate 0.5 and 4 Hz. **k**, Area under the curve (AUC) for DA power in 0.5–4 Hz band in control (n = 13), sulpiride-treated ($p = 1.2\times10^{-12}$; n = 8) and 6OHDA-lesioned ($p = 1.1\times10^{-9}$; n = 6) mice (all vs. control, Student's two-sample *t*-test). **l-o**, Same as **h-k** for ACh3.0 in control (n = 13), scopolamine-treated ($p = 3.0\times10^{-6}$; n = 5), and ChAT $cKO^{forebrain}$ ($p = 8.3\times10^{-6}$; n = 5) mice. Group means (± s.e.m.) in **g**, **k** and **o** are shown in black. Shaded area in **e**, **f**, **i**, **j**, **m** and **n** depicts s.e.m.

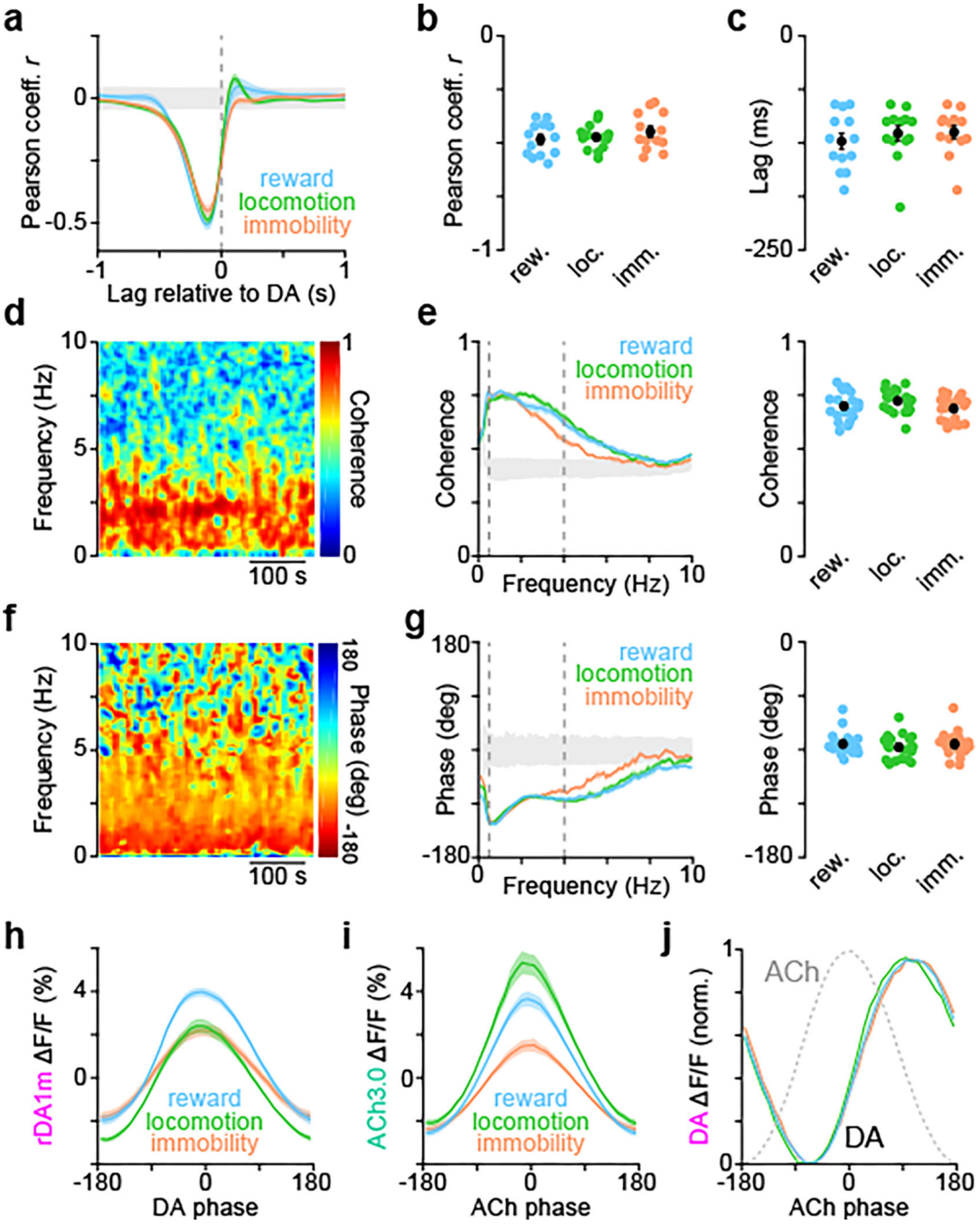

Fig. 2. DA and ACh maintain a consistent temporal relationship across behavioral states.

a, Mean cross-correlation between simultaneously recorded DA and ACh signals (n = 13 mice) during reward (blue), locomotion (green) and immobility (orange). Gray: 95% confidence interval. **b,** Peak correlation coefficient between DA and ACh across behavioral states (p = 0.5, one-way balanced ANOVA; n = 13 mice). **c,** Same as **b** for time lag of negative cross-correlation peak (p = 0.6). **d,** Example coherence between DA and ACh signals across frequency and time domains. **e,** *Left*, mean coherence between DA and ACh at different frequencies across behavioral states (n = 13 mice). Vertical lines depict 0.5 and

4 Hz. *Right*, median coherence in 0.5–4 Hz band in individual mice (p = 0.9, one-way balanced ANOVA). **f-g,** Same as **d-e** for phase offset between DA and ACh (p = 0.6). **h,** Mean DA fluorescence at different phases of periodic DA fluctuations in the 0.5–4 Hz frequency band. **i,** Same as **h** for ACh fluorescence. **j,** Peak-normalized DA fluorescence vs. phase of periodic ACh fluctuations (gray dotted line) in 0.5–4 Hz band during reward (blue), locomotion (green) and immobility (orange). Group means (± s.e.m.) in **b**, **c**, **e** and **g** are shown in black. Shaded area in **a, e, g, h-j** depicts s.e.m.

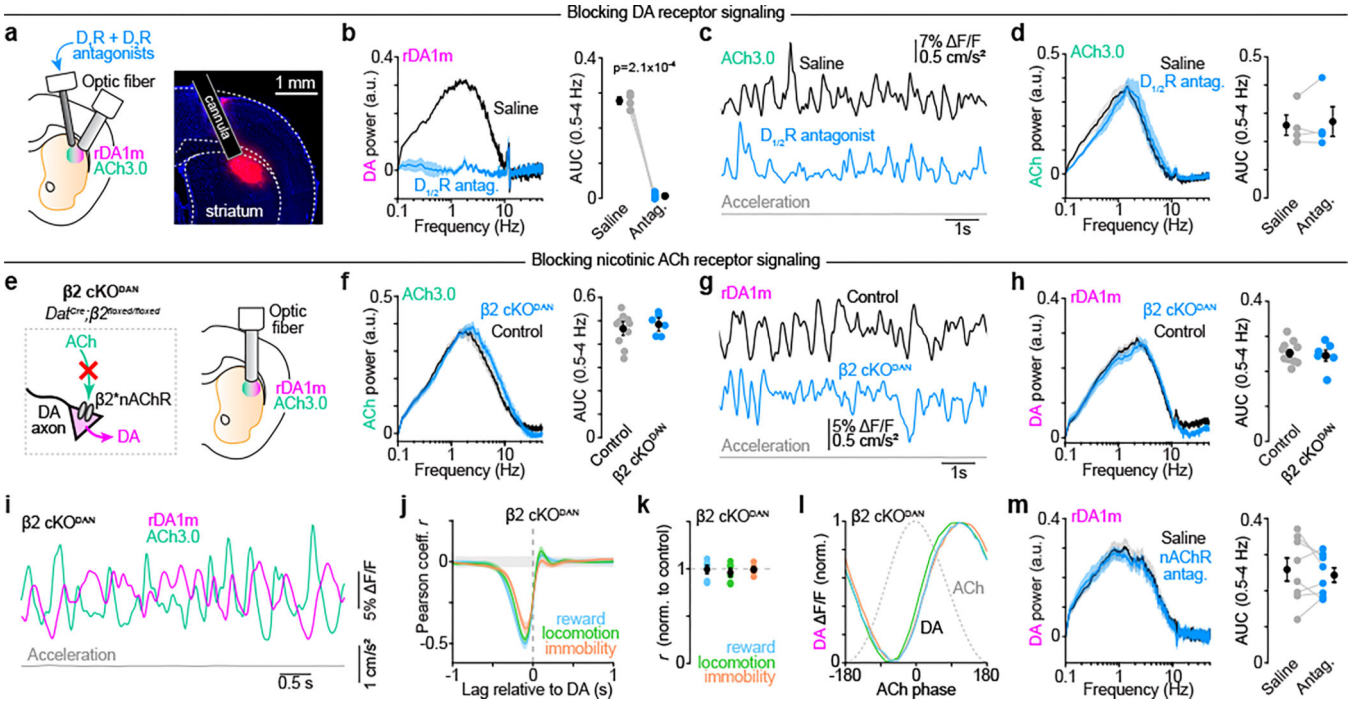

Fig. 3. Periodic DA and ACh fluctuations are not coordinated locally in the striatum.

a, *Left*, experimental preparation. *Right*, drug diffusion estimate using fluorescent dye in one of 3 similar experiments. **b**, Mean DA power spectrum (*left*) and area under the curve (AUC) in 0.5–4 Hz band (*right*; p = 2.1×10^{-4}, Student's paired *t*-test; n = 4 mice) during immobility after intra-striatal infusion of saline (black) or D1/2R antagonists (blue). **c**, Example ACh3.0 recording in saline or D1/2R antagonists. **d**, Same as **b** for ACh (p = 0.35). **e**, Strategy for genetically ablating ACh-evoked DA release from DANs. **f**, Same as **b** for ACh power in control (black; n = 13) and β2 cKO^{DAN} (blue; n = 6) mice during immobility (p = 0.5, Student's two-sample *t*-test). **g**, Example DA fluctuations in control and β2 cKO^{DAN} mice. **h**, Same as **f** for DA power (p = 0.2). **i**, Example DA (magenta) and ACh (teal) traces from a β2 cKO^{DAN} mouse. **j**, Mean DA–ACh cross-correlogram during reward (blue), locomotion (green) and immobility (orange) in β2 cKO^{DAN} mice. Gray: 95% confidence interval. **k**, Pearson correlation coefficient *r* between DA and ACh in six β2 cKO^{DAN} mice normalized to control mice during reward (p = 0.6), locomotion (p = 0.9) and immobility (p = 0.4; all vs. control, Student's two-sample *t*-test). **l**, Peak-normalized DA fluorescence in β2 cKO^{DAN} mice vs. phase of periodic ACh fluctuations in 0.5–4 Hz band. **m**, Same as **b** for DA power following intra-striatal infusion of saline or the nAChR antagonist DHβE (p = 0.5, Student's paired *t*-test; n = 8 mice). Group means (± s.e.m.) in **b**, **d**, **f**, **h**, **k** and **m** are shown in black. Shaded area in **b**, **d, f, h, j** and **m** depicts s.e.m.

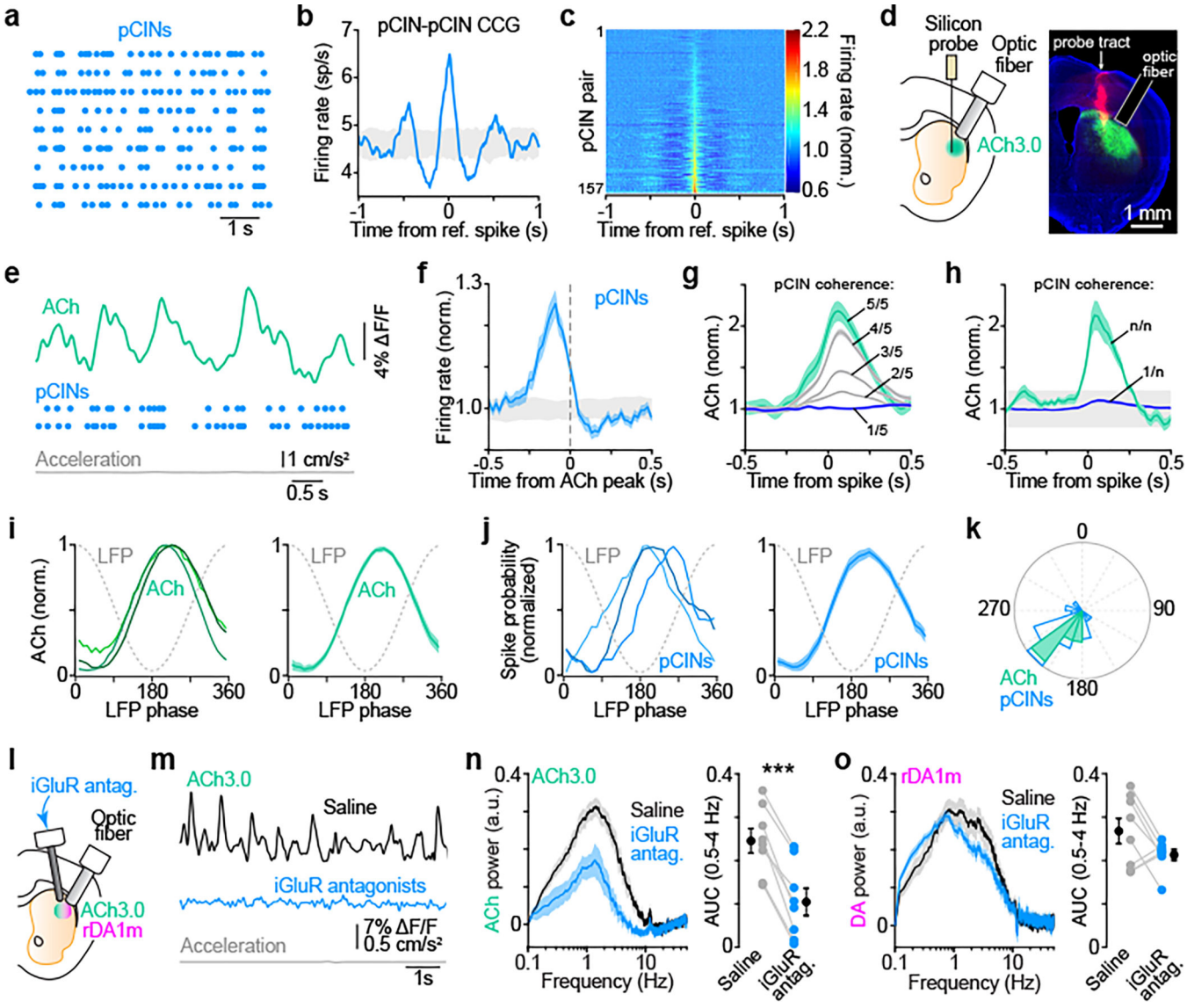

Fig. 4. Glutamatergic inputs synchronize CIN spiking and drive periodic ACh fluctuations.

a, Spike raster of 9 putative (p) CINs recorded simultaneously in the DLS during immobility. **b**, Spike cross-correlogram (CCG) between two units in **a**. **c**, Heatmap of spike CCGs for all pCIN pairs (n = 157) normalized to mean firing rate during immobility. **d**, Experimental configuration (*left*) and representative coronal section (*right*) from 4 similar mice showing the silicon probe track (red) near the fiber optic used to image ACh3.0. **e**, Example simultaneous recording of ACh levels (teal) and spiking from 2 pCINs (blue) during immobility. **f**, Average pCIN firing rate (mean-normalized) aligned to peaks in ACh3.0 fluorescence (n = 22 units). **g**, Example pCIN spike-aligned ACh signal stratified based on the fraction of concurrently-recorded pCINs that are co-active. **h**, Mean pCIN spike-aligned ACh3.0 fluorescence when only 1 (blue) or all (teal) concurrently-recorded pCINs are co-active. **i**, Three examples (*left*) and average (n = 4 mice; *right*) peak-normalized ACh signal aligned to the phase of striatal LFP oscillations in the 0.5–4 Hz band. **j**, Same as **i** for spike probability in 52 out of 55 pCINs (94.5%) that showed a significant

phase relationship to 0.5–4 Hz LFP. **k**, Polar plot of preferred phase of individual pCINs (blue) and ACh recordings (teal) relative to 0.5–4 Hz LFP. **l**, Experimental configuration. **m**, Example ACh fluctuations during immobility following intra-striatal infusion of saline (black) or iGluR antagonists (blue). **n**, Mean ACh power spectrum (*left*) and area under the curve (AUC) in 0.5–4 Hz band (*right*; $p = 2.2\times10^{-5}$, Student's paired *t*-test; n = 8 mice) during immobility. **o**, Same as **n** for DA (p = 0.10). 95% confidence interval in **b**, **f** and **h** is shown in gray. Shaded area in **f**-**j**, **n** and **o** depicts s.e.m.